Climate Data Record (CDR) Program

Climate Algorithm Theoretical Basis Document (C-ATBD)

AVHRR Cloud Properties – PATMOS-x

Daytime Cloud Optical and Microphysical Properties (DCOMP)

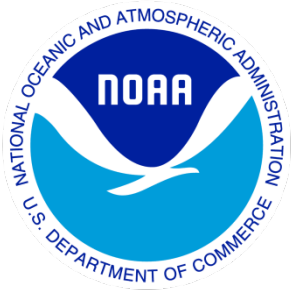

CDR Program Document Number: CDRP-ATBD-0523
Configuration Item Number: 01B-01b
Revision 1 / March 17th, 2014

REVISION HISTORY

Rev.	Author	DSR No.	Description	Date
1	Andi Walther, CIMSS/UW-Madison	DSR-654	Initial Submission to CDR Program	03/17/2014

TABLE of CONTENTS

LIST of FIGURES

LIST of TABLES

1. Introduction

1.1 Purpose

This climate algorithm theoretical basis document (C-ATBD) for Daytime Cloud Optical and Microphysical Properties (DCOMP) provides a high-level description of the physical basis for inferring cloud optical depth (COD), cloud particle size (CPS), liquid water path (LWP) and ice water path (IWP). The COD and CPS will be inferred for all pixels identified as containing cloud by the cloud mask. We distinguish clouds as either ice phase or water phase. The latter also include in our definition super-cooled and mixed phase clouds. The COD and CPS are used subsequently to calculate liquid/ice water path (LWP/IWP), whose values can be compared with those, derived from active measurements from space-born instruments such as the Cloud Profiling Radar (CPR) on CloudSat and passive microwave sensors such as AMSR-E or SSM/I, as well as ground-based microwave profilers. The intended users of this document are those interested in understanding the physical basis of the algorithms and how to use the output of this algorithm to study or assimilate cloud properties. This document also provides information useful to anyone maintaining or modifying the original algorithm.

1.2 Definitions

Following is a summary of the symbols used to define the algorithm.

Table 1 Parameters and mathematical symbols used.

Parameter	Symbol	Typical Value
Reflectance (at top of atmosphere, top of cloud)	$R \quad (R_{TOA}, R_{TOC})$	0.4
Reflectance backscattered to sensor	R_{sc}	0.1
Transmittance function (above, below cloud)	$T(T_{ac}, T_{bc})$	0.95
.. through water vapor including trace gases	T_{h2o}	0.91
.. through ozone, aerosol, air molecules	T_{o3}, T_{aer}, T_r	0.93
.. for cloud, downward, cloud upward	T_c, T_c^*	0.8,0.8
Local zenith angle, cosines of	$\theta, \ \mu$	34, 0.7
Solar zenith angle, cosines of	$\theta_0, \ \mu_0$	34, 0.7
Relative azimuth difference	$\Delta\varphi$	120
Optical depth for clouds, Rayleigh, aerosol	$\tau_c, \tau_r, \tau_{aer}$	12 0.03 0.05

Background optical depth for Rayleigh, aerosol	$\tau_{r,0}, \tau_{aer,0}$	0.044 0.1
Cloud, particle radius, Effective radius	r, r_e	10 μm
Cloud droplet number distribution	$n(r)$	1000
Phase function	P	0.3
Rayleigh phase function	P_r	0.2
Scattering angle	ζ	123 deg
Cloud albedo	A_c	0.4
Spherical cloud albedo	R_c^*	0.1
Azimuthal averaged reflectance	R^*	0.1
Air mass factor	AMF	2.9
Asymmetry parameter	g	0.7
Single-scattering albedo	ω_0	1
Surface pressure, cloud top pressure	p_{sfc}, p_c	540hPa 1013hPa
Solar radiation	I	
Surface Albedo	A_{sfc}	0.08
Water vapor mass	u_{H_2O}	0.17 dm
Ozone mass	u_{O_3}	382 Dobson

1.3 Referencing this Document

This document should be referenced as follows:

AVHRR Cloud Properties – PATMOS-x (DCOMP) - Climate Algorithm Theoretical Basis Document, NOAA Climate Data Record Program CDRP-ATBD-0523 by CDRP Document Manager Rev. 1 (2014). Available at http://www.ncdc.noaa.gov/cdr/operationalcdrs.html

1.4 Document Maintenance

Any update to the DCOMP algorithm that would affect files hosted by the CDR Program would initiate a revision and redelivery of the DCOMP C-ATBD document.

2. Observing Systems Overview

2.1 Products Generated

The DCOMP algorithm is responsible for generating the DCOMP products, which are cloud optical depth (COD) and cloud particle size (CPS) for all daytime pixels that are detected as cloudy. Subsequently liquid water path (LWP) and ice water path (IWP) products will be derived from COD and CPS.

COD represents the vertical optical thickness between the top and bottom of an atmospheric column. COD is almost independent of wavelength in the visible range of the spectrum. COD has no unit. CPS is supposed to represent the cloud droplet distribution. The cloud effective radius (REF), defined as the ratio of the third to the second moment of a droplet size distribution, is well suited to fulfill this task. CPS has the unit micrometer (μm).

LWP and IWP are a measure of the total mass of water in a cloud column. The unit is gram per square meter (g/m2).

In our context, "daytime" is defined to be where the solar zenith angle for a given pixel is less than or equal to 65 degrees, for which DCOMP provides full quality products. To fill a temporal gap between DCOMP and the nighttime cloud properties algorithm (NCOMP) degraded products for solar zenith angles between 65 and 82 degrees will be provided by DCOMP.

The current cloud mask design has four categories: clear, probably clear, probably cloudy and cloudy. The DCOMP products will be derived for pixels that are probably cloudy or cloudy

2.2 Instrument Characteristics

The DCOMP algorithm was developed with funding from the Advanced Baseline Imager (ABI) on the Geostationary Operational Environmental Satellite (GOES) series, to be launched with the GOES-R satellite. As a result, many of the figures and validation found in this document are based on Spinning Enhanced Visible and Infrared (SEVIRI) measurements designed as a proxy for ABI. The PATMOS-x Cloud TCDR for which this document was adapted is derived from the Advanced Very High Resolution Radiometer (AVHRR) instruments that fly on the NOAA and EUMETSAT polar orbiters. The AVHRR instruments have five channels (with channel 3 being split between two wavelengths), each with a nadir pixel spatial resolution of 1.09 kilometers. The Global Area Coverage (GAC) data, from which the PATMOS-x record is generated, averages 4 pixels from the center of a 3x5 pixel array; meaning the spatial resolution is approximately 4 kilometers at nadir. An important difference between the ABI and AVHRR in the context of the DCOMP algorithm is that ABI uses a 2.26 μm channel for particle size retrieval, while the AVHRR uses the 3.75 μm channel. Table 2 shows the ABI and AVHRR channels and identifies those used in the DCOMP algorithm.

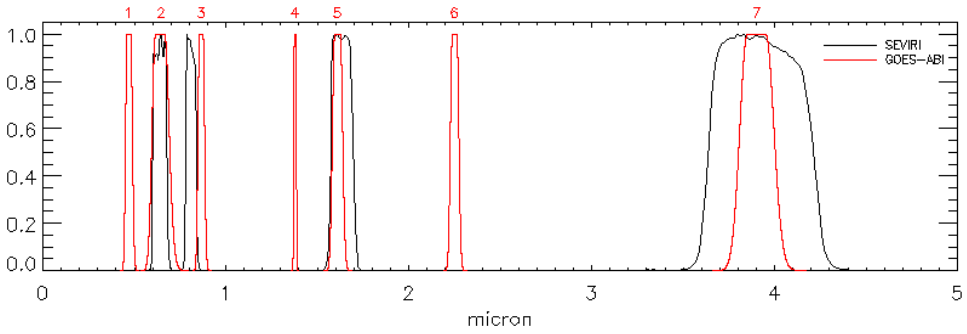

Figure 1. Channel spectral response function for GOES-ABI (red) and the current sensor SEVIRI onboard METEOSAT in the visible and near-infrared spectrum.

Figure 1 shows the spectral response functions of GOES-ABI in the visible and near-infrared part of the spectra. This image also indicates that the SEVIRI sensor onboard the European geostationary satellite system METEOSAT Second Generation (MSG) has only slightly different response functions for GOES ABI channels 2, 5 and 7. Therefore, SEVIRI is well suited to provide proxy data to test the GOES ABI algorithm before launch. Table 1 summarizes the channel settings used by the DCOMP approach.

Table 2 Channel numbers and wavelengths for AVHRR and ABI and the usage within the retrieval.

ABI Channel Number	Wavelength range (μm)	Used for the algorithm	AVHRR Channel Number	Wavelength range (μm)	Used for the algorithm
1	0.45-0.49 (0.47)				
2	0.59-0.69 (0.64)	✓	1	0.58-0.68 (0.63)	✓
3	0.846-0.885 (0.865)		2	0.725-1.00 (0.86)	
4	1.371-1.386 (1.378)				
5	1.58-1.64 (1.61)		3a	1.58-1.64 (1.61)	
6	2.225-2.275 (2.25)	✓			
7	3.80-4.00 (3.9)		3b	3.55-3.93 (3.75)	✓
8	5.77-6.60				

	(6.15)				
9	7.0				
10	7.4				
11	8.5				
12	9.7				
13	10.35				
14	11.2		4	10.30-11.30 (10.80)	
15	12.3		5	11.50-12.50 (12.00)	

3. Algorithm Description

3.1 Algorithm Overview

DCOMP is based on earlier methods that retrieve cloud optical depth and cloud effective radius from visible and near-infrared wavelengths [*Nakajima and King*, 1990] [*King*, 1987; *Nakajima and King*, 1992]. To briefly describe the underlying idea of the retrieval, cloud optical depth, referred to absorption-free wavelengths (for instance to 550 nm), is determined by the amount of light scattering by cloud droplets. The size of the droplets is responsible for absorption and the transition to a new direction of scattered photons, expressed by the phase function $P(\zeta)$, which is a function of the scattering angle, ζ . Since the effective radius (REF) is a measure of the volume of cloud particles, it is mirrored in absorption amount of clouds. The basic premise is that COD and REF are inferred from solving the radiative transfer equation for a single-layered, plan-parallel homogeneously distributed cloud above a Lambertian surface. The retrieval concept is based on a 1D radiation concept where a cloud completely covers a pixel. The DCOMP algorithm uses an absorption-free channel to retrieve the cloud optical depth by measuring upward backscattered radiance and uses an absorption solar channel to estimate particle size through the observed amount of absorption. Simultaneous measurements are required since estimating optical depth from backscattered signals requires the phase function. The amount of absorption cannot be separated from extinction by scattering without measurements in a conservative channel, such as the AVHRR channel 1 or ABI channel 2. The cloud optical thickness and cloud particle size are retrieved from measurements of the AVHRR channels 1 and 3b centered in the visible spectra at $\lambda_{VIS} = 0.63\mu m$ and in the near-infrared spectra at $\lambda_{NIR} = 3.75\mu m$. GOES-ABI uses channels 2 and 6 centered in the visible spectra at $\lambda_{VIS} = 0.64\,\mu m$ and in the near-infrared spectra at $\lambda_{NIR} = 2.25\mu m$. The channel pair $\lambda_{VIS} = 0.64\mu m$, $\lambda_{IR} = 1.60\mu m$ was applied during the pre-launch phase to the test data set of SEVIRI measurements.

3.2 Processing Outline

The processing outline of the DCOMP is summarized in Figure 2. The daytime DCOMP algorithm is designed to run on segments of data where a segment is comprised of multiple scan lines.

The current DCOMP algorithm can be implemented in several frameworks, including that used by PATMOS-x, CLAVRX. This system provides all primary sensor inputs and ancillary data and generates the output files. The DCOMP algorithm can run on segments of data, as all cloud algorithms do, but can also run on individual pixels if all of the input data and ancillary data sets are available.

The DCOMP retrieval needs the following products from other retrievals: cloud mask, cloud top pressure and cloud phase. Under the current processing structure the generation of these products is done in the same process unit in a pre-defined order in advance to the DCOMP retrieval for each segment. The actual DCOMP retrieval starts at the first call (segment) with testing the channel settings and loading all LUTs and the coefficients for water vapor correction in memory. The memory will be freed after the last scan line is completed.

There is one kind of look-up-tables to be read in. The cloud LUTs include reflection, transmittance, cloud albedo and cloud spherical albedo tables. The data from the LUTs are accessed via an auxiliary library with a *get_lut_data* subroutine.

For each segment a measure for spatial homogeneity is calculated, and surface albedo values are read into a local variable. Afterwards, the pixel-by-pixel loop begins with several validity tests and the aliasing of framework parameters to local pointers in the subroutine *assign_local_var*. The tests reject pixels that (1) look into space, are outside valid sensor and sun angle range, are (2) cloud-free, or (3) have no valid cloud pressure or cloud phase. If the input data pass each test, the program sets alias variables for all primary and ancillary input data valid for the current pixel.

Subsequently, atmospheric corrections are executed for the cloud-free layers above and below the cloud (*atmospheric_correction* subroutine). We correct the atmosphere for the upper layer by estimating the real top-of-cloud reflectance by adjusting the TOA measurement, and by estimating a virtual surface albedo that includes atmospheric extinction for the atmosphere below the cloud. In this way, an observation vector $\boldsymbol{y}$ is defined as the input of the inversion through an optimal estimation technique with a modified surface albedo. The result of the inversion is a COD/CPS pair from which the liquid water path or ice water path will be calculated, respectively. Those four products and a common quality flag are stored in the output arrays.

Within the retrieval loop (*optimal_estimation see* Figure 3), an iterative 1D-var optimal estimation technique is applied (OE). It starts with the definition of a priori values of the state vector and the appropriate observation and atmospheric state covariance matrices. The cost will be calculated for each iteration step. The cost parameter updated at each iteration is initialized with the biggest possible value for this data type (cost = HUGE() for FORTRAN). Each iteration step of the retrieval loop requires search events in the LUTs. Comparison of the TOC reflectance (the observation vector), derived by the forward model represented by the LUTs, to the measurement defines a cost surface function. The OE algorithm's task is to find the minima value on this surface. The gradient of the cost serves as a compass pointing downhill to the deepest point. The a priori values can be seen as a weighting function for the cost surface and help to speed up the state vector journey.

If the cost falls below a pre-defined threshold, the solution is found and the retrieval loop will end. Otherwise, if a maximal number of iterations is exceeded, no solution could be found. The quality flag gets a corresponding value.

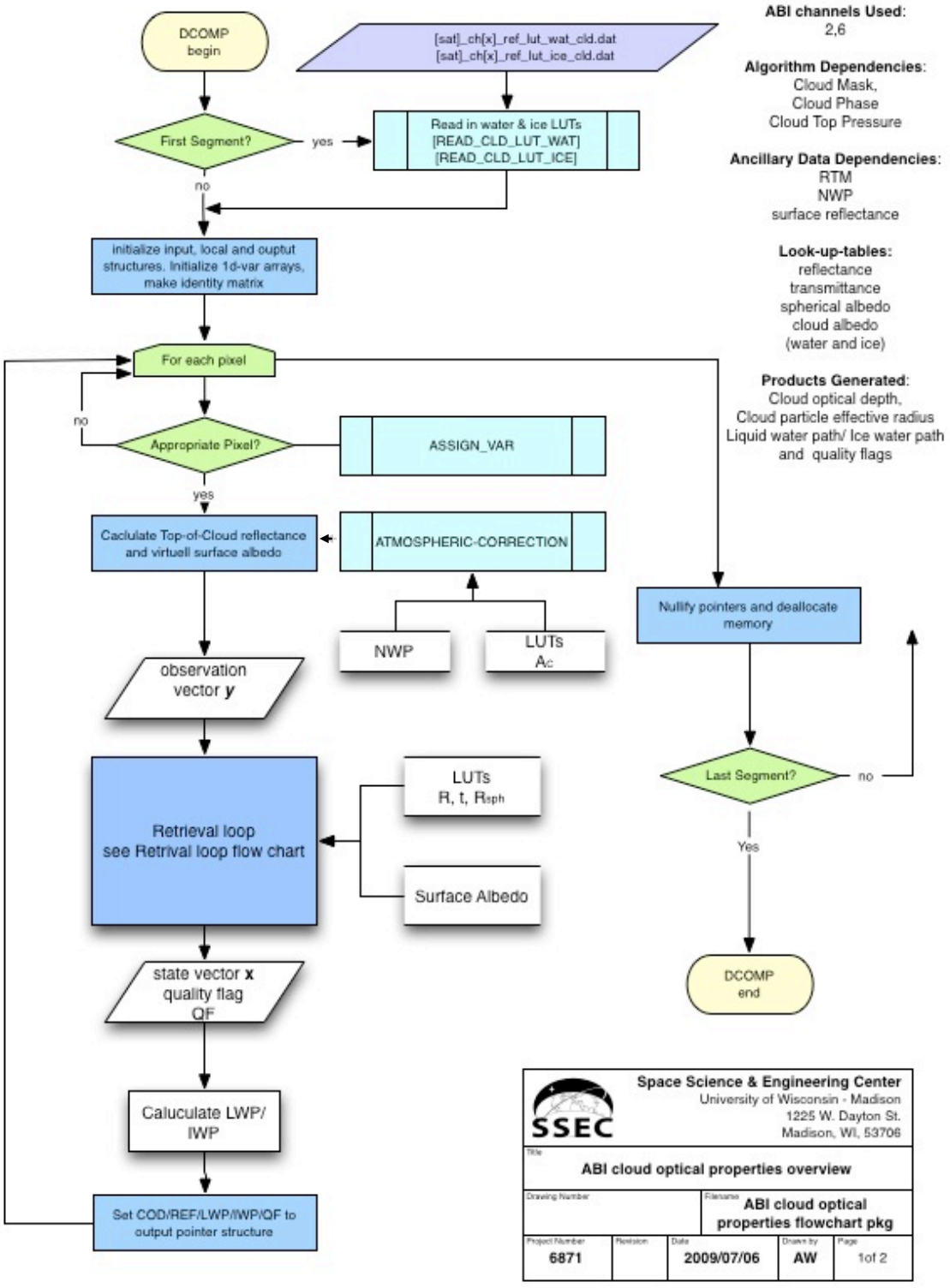

Figure 2. High-level flowchart of the COP/CPS algorithm

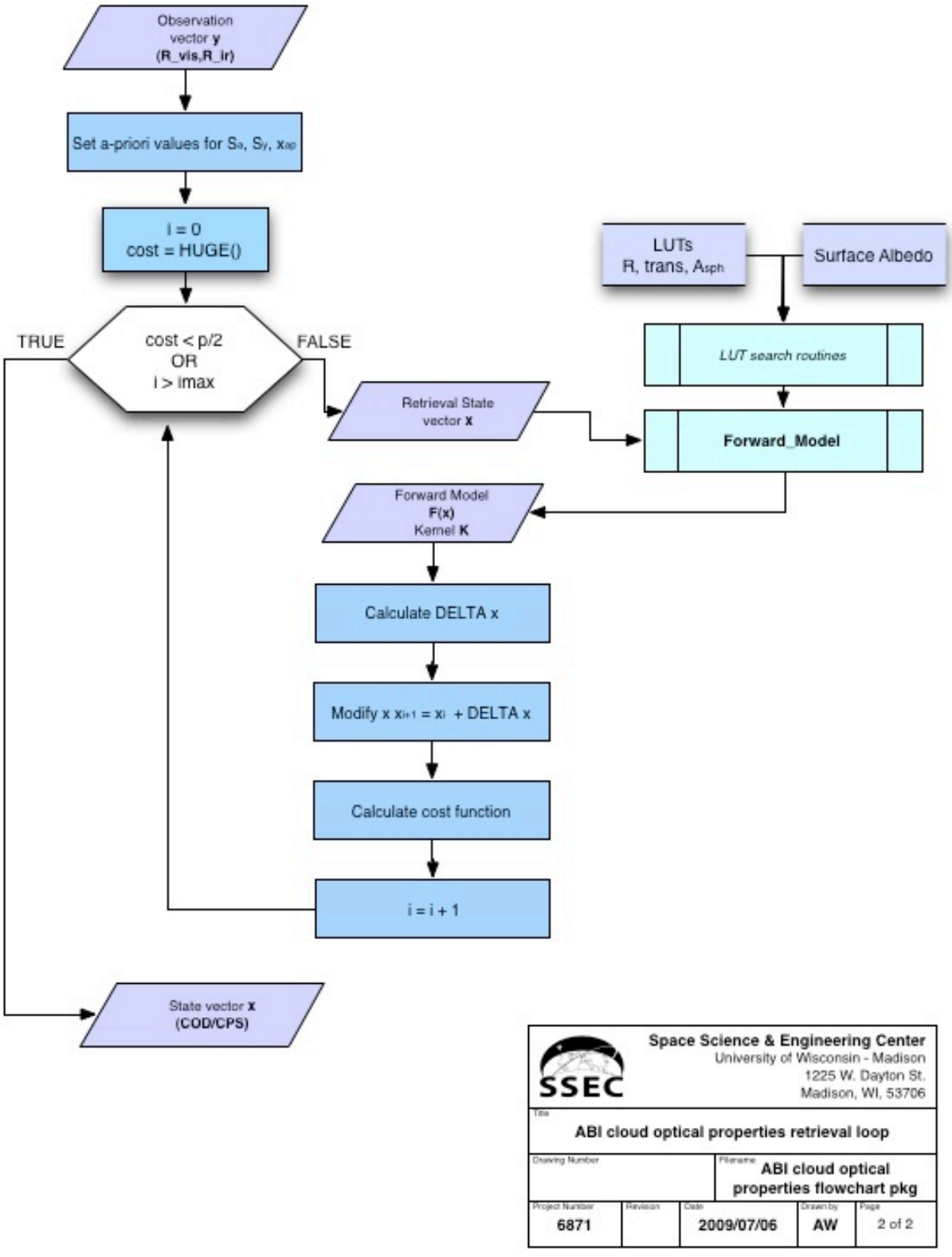

Figure 3: Flow chart of retrieval loop.

3.3 Algorithm Input

3.3.1 Primary Sensor Data

The list below contains the primary sensor data used by DCOMP retrieval. Primary sensor data refers to information that is derived solely from the observations and its associated geo-location information. The DCOMP algorithm uses calibrated reflectance percent (0-100) as input. However, inside the algorithm, the input is converted to calibrated reflectance (0-1), which is reflectance percent / 100.

Table 3 Primary sensor input

Name	Type	Description	Dimension
VIS reflectance	Input	Calibrated reflectance in a visible channel at around 0.63 micron	grid (xsize, ysize)
NIR reflectance	Input	Calibrated radiance in channel around 3.75 micron	grid (xsize, ysize)
Latitude	Input	Pixel latitude	grid (xsize, ysize)
Longitude	Input	Pixel longitude	grid (xsize, ysize)
Solar geometry	Input	Solar zenith and azimuth angles	grid (xsize, ysize)
View geometry	Input	View zenith and azimuth angles	grid (xsize, ysize)

3.3.2 Ancillary Data

The following lists the ancillary data required to run the DCOMP algorithm in the PATMOS-x AVHRR climate record. By ancillary data, we mean data that requires information not included in the observations or geolocation data. Ancillary data includes data such as land and snow masks, Numerical Weather Prediction (NWP) or reanalysis data (as used here) and RTM data as well as the lookup tables (LUT) that are used in the forward model calculations. The reanalysis and RTM data, which are at reanalysis resolution, are interpolated to pixel level. The snow mask is derived from the CFSR , which is interpolated to pixel level. Table 4 lists the non-LUT data, which are used in DCOMP. Table 5 lists the NWP data that are used in DCOMP and Table 6 lists the information in the DCOMP LUT.

- **Land mask**
- **Surface clear sky reflectance (Albedo)**
- **Snow Mask**

- **Climate Forecast System Reanalysis (CFSR)**: CFSR 6-hourly data are used to estimate the absorber mass for atmospheric correction of water vapor and ozone absorption and the determination of surface pressure for aerosol and Rayleigh correction. DCOMP uses the same ancillary data as all cloud algorithms. CFSR data are transformed to the grid outside the DCOMP algorithm in the full processing scheme in the framework.
- **Look-up-tables:** Look-up-tables are provided for cloud properties and for transmission coefficients. The LUTs will be generated in advance and are static ancillary data. Cloud properties LUT set consists of four data files for ice and water phase and for both channels. Transmission coefficients are provided in one LUT file.

Table 4 Non-LUT ancillary data.

Name	Type	Description	Dimension
Land mask	input	Land –sea mask	1 km
Surface reflectance	input	MODIS white sky albedo	1 km
Snow Mask	input	CFSR derived snow mask	1km

Table 5 CFSR input data

Name	Type	Description	Dimension
Pressure profile	input	Pressure profile with *nlev* number of levels	grid (xsize, ysize,nlev)
Temperature profile	input	Temperature profile with *nlev* number of levels	grid (xsize, ysize,nlev)
Water vapor profiles	input	NCEP Water vapor profile data with *nlev* number of levels	grid (xsize, ysize, nlev)
Ozone amount	input	NCEP ozone amount data	grid (xsize, ysize)
Surface Pressure	input	NCEP surface height data	grid (xsize, ysize)

Table 6 LUT ancillary data

Name	Type	Description	Dimension
Cloud properties LUT	Input	Cloud reflectance as a function of effective radius, optical depth, solar zenith angle, local zenith angle and relative azimuth difference angle	(9 x 29 x 45 x 45 x 45)

		Cloud transmission as a function of effective radius, cloud optical depth and incoming angle	(9 x 29 x 45)
		Cloud spherical albedo as a function of effective radius and cloud optical depth	(9 x 29)
		Cloud albedo as a function of effective radius and cloud optical depth and incoming angle.	(9 x 29 x 45)

3.3.3 Derived Data

The following lists and briefly describes the data that are required by DCOMP that are provided by other algorithms.

- **Cloud mask:** A cloud mask is required to determine which pixels are cloudy and which are cloud free, which in turn determines which pixels are processed. The ABI Cloud Mask (ACM) algorithm provides this information.
- **Cloud top pressure:** Cloud top pressure is required to determine the amount of absorber mass by water vapor above the cloud for atmospheric correction. This information is provided by the ABI Cloud Height (ACHA) algorithm.
- **Cloud phase:** Cloud phase is required to determine which LUT, ice or water is used for forward model calculations. This information is provided by the ABI Cloud type/Phase algorithm.
- **Snow mask:** Using the snow mask, each pixel is flagged internally as snow or clear. In addition, if a pixel has an 11 μm brightness temperature of greater than 277K, the snow mask is turned off.

3.3.4 Forward Models

3.3.4.1 Forward model in near-infrared channel around 3.75 micron

If DCOMP is applied to sensor channels around 3.8 microns (such as AVHRR channel 3b, SEVIRI channel 4, GOES channel 2 or MODIS channel 20) terrestrial emission must be taken into account. The term R_{TOC} in depicts the solar reflectance. However, for these channels the measured radiance is a sum of backscattered solar radiation and a terrestrial emission part.

The latter is the top of cloud radiance I_{TOC} , which is emitted from the surface and atmosphere. This can be expressed as

$$I_{TOC} = \varepsilon(\tau, r_e) B_c(T_c) + t_c(\tau, r_e)(I_{clr} - I_a(H)) \qquad (1)$$

where I_a is the radiance contribution from layers above the cloud height H, I_{clr} is the clear-sky radiance emitted by the surface, ε_c is the cloud emissivity, t_c is the cloud transmission, and B(T_c) is the Planck function at the cloud top temperature T_c. Cloud emissivity $\varepsilon(\tau, r_e)$ and cloud transmission $t_c(\tau, r_e)$ are computed by the radiative transfer model and stored in look-up-tables. They depend on the state vector, so that they are optimized during the retrieval loop. The other unknown variables of equation 1 are obtained from auxiliary data as follows. The new National Center of Environmental Prediction (NCEP) Climate Forecast System Reanalysis (CFSR) (Kalnay et al. 1990; Saha et al. 2010; Sela 1980) provides realistic atmospheric profiles of temperature and water vapor on global regular 0.5 and 2.5 degree grid from 1979 onwards. We employ a fast IR radiative transfer code, the Pressure-Layer Fast Algorithm for Atmospheric Transmittances PFAAST (Hannon 1996) with the input from these reanalysis, combined with surface emissivity values obtained from a MODIS-based database (Seemann et al. 2008) to compute assumed clear-sky radiance and transmission profiles.

Cloud top temperature and cloud top height are obtained from the NOAA Algorithm Working Group (AWG) Cloud Height retrieval Algorithm (ACHA), which is also part of PATMOS-x retrieval scheme, in which it runs in advance of DCOMP.

Subsequently, the terrestrial radiance I can be transformed into an equivalent reflectance value R_e as follows:

$$R_{e,TOC} = \frac{\pi d^2}{\mu_0 F_0} I_{TOC} \qquad (2)$$

where d is the Earth-Sun distance in astronomic units (AU) and F_0 is the channel-specific solar constant normalized to the average Earth-Sun distance using the Kurucz solar irradiance database (Kurucz 1995). The solar part of the measured reflectance are extracted by

$$R_{TOC} = R_{mea} - R_e \qquad (3)$$

Through including the terrestrial emissivity observed at top of cloud, Eq. (3) becomes an equation for each measurement channel:

$$R_{TOC} = R_c(\tau, r_e) + \frac{A_v t_{c,0}(\tau, r_e) t_c(\tau, r_e)}{1 - A_v S(\tau, r_e)} + R_{e,TOC}(\tau, r_e) \qquad (4)$$

This is in fact a general equation for any channel. For the visible to near-infrared spectral range, the amount of radiance, which comes from surface or atmospheric emission, is negligible, and $R_{e,TOC}$ becomes zero.

Now all formulations are prepared to proceed to the inversion problem, which aims to find the pair of cloud properties (τ, r_e). At the end of this process the retrieval will find a pair of the cloud properties (τ, r_e) that satisfy the equations. The problem is not analytically solvable due to the complicated nature of radiative transfer.

3.4 Theoretical Description

3.4.1 Physical and Mathematical Description

This section describes the mathematics used by the retrieval, including all simplifications, approximations, and numerical methods. This section is divided in the description of the LUTs as the representation of a forward model, the correction of atmospheric impacts on the measured input data, and the inversion method.

3.4.1.1 Basic Considerations

Cloud radiation characterizations in the shortwave range of the infrared spectrum are almost exclusively a function of cloud optical depth (also referred to as cloud optical thickness) and the cloud droplet distribution n(r), which can be represented by the integral of the third moment over the second moment of the distribution of particle size, the effective radius r_e [*Hansen and Travis*, 1974]:

$$r_e = \frac{\int r^3 n(r)\mathrm{d}r}{\int r^2 n(r)\mathrm{d}r} \qquad (5)$$

It has been shown that the effective radius represents adequately the radiative properties of a cloud, which are largely independent to the shape and width of the droplet distribution. The values of effective radius vary usually between $r_e = 3\mu m$ and $r_e = 40\mu m$ for liquid cloud phase and up to $r_e = 100\mu m$ for ice clouds. As a simplification, cloud optical depth determines the quantity of scattering processes, while cloud droplet size is responsible for redistributing the direction of the scattering processes, expressed as the phase function P(r). Cloud optical depth and effective radius are often used for the characterization of clouds in global climate models. Both together describe completely the backscatter signature of a cloud.

For the retrieval instead of a measured direct solar reflected radiance *L* [$Wm^{-2}nm^{-1}sr^{-1}$], we use a measure of reflectivity R for each wavelength. Those values may

be calculated under consideration of the spectral solar constant F_0 [$Wm^{-2}nm^{-1}$], the sun zenith angle θ_0 and the local zenith angle θas

$$R(\theta_0,\theta,\lambda)=\frac{\pi L(\theta_0,\theta,\lambda)}{F_0(\lambda)\cos\theta_0} \qquad (6)$$

By using R instead of L we avoid an overestimation of shortwave channels, where the solar irradiance is bigger than for longer wavelengths.

Cloud optical depth represents optical characterization at visible wavelengths and can be expressed as a function of the scattering coefficient Q, the droplet size distribution $n(r)$ and the droplet radius r:

$$\tau=\int n(r)Q(r,\lambda)\pi r^2\,\mathrm{d}r \qquad (7)$$

The cloud liquid water path may be derived with the cloud optical thickness and the droplet effective radius estimates using the following equation [*Stephens*, 1978] , [*Bennartz*, 2007]

$$LWP=\frac{5}{9}\tau_c r_e \rho \qquad (8)$$

where ρ is the density of liquid water.

The ice water path (IWP) can be derived by (Heymsfield, 2003):

$$IWP=\frac{\tau_c^{1/0.84}}{0.065} \qquad (9)$$

This relationship fits the observations for several locations and experiments, but may lead to big differences in comparison to traditional methods which use a small dependency to cloud particle size similar to the equation for liquid phase. Figure 4 shows big differences in the retrieved IWP product for different methods.

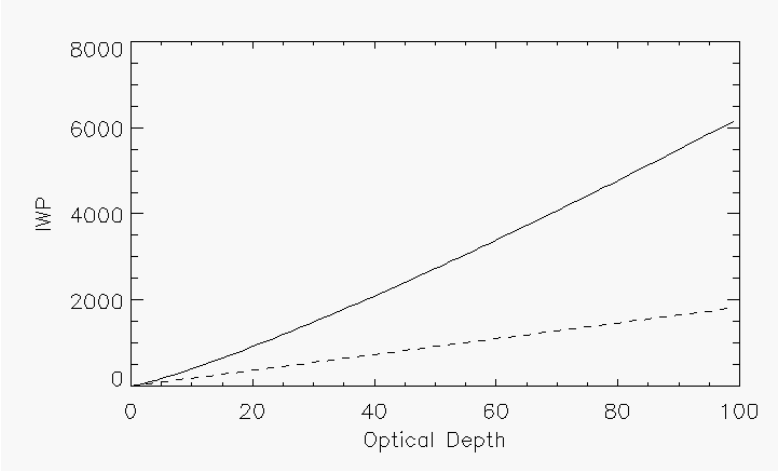

Figure 4. Comparison of Heymsfield method to a traditional method (dashed line) of calculating the ice water path from optical depth.

It has been shown that using two channels in the visible and near infrared spectrum is sufficient to retrieve both parameters (King 1987, Nakajima und King 1991). The underlying principle on which these methods are based is the fact that the cloud reflectance at visible wavelengths is primarily a function of the cloud optical thickness, while the variations in the measured reflectance in the near infrared water-absorbing channels are mostly affected by the particle size.

The basic premise is that DCOMP is inferred from solution of the radiative transfer equation for a single-layered, homogeneously distributed cloud above a Lambertian (isotropic) surface. A cloud with a given optical thickness and cloud effective particle size can be described by its reflectance/transmittance functions. To speed up the process for operational retrievals, the reflectance/transmittance functions for both ice and water clouds are pre-calculated and stored in look-up tables (LUTs). Further description of the process used to develop the LUTs is given in the following section, as is the methodology to use the LUT to infer COD/CPS.

3.4.1.2 Radiative Transfer Calculations

To simulate the radiative properties of a cloud, a doubling-adding model is used. In this model the atmosphere comprises three layers, two cloud-free layers and a cloud layer in between. The doubling-adding method to solve radiative transfer problems is widely used in the scientific community. Van de Hulst developed this technique. It generates fast and accurate estimates of light distribution in a cloudy atmosphere. It assumes knowledge of the reflection and transmission properties for a single thin homogeneous atmosphere layer. The basic principles can be found in several publications, such as Goody and Young van de Hulst or Thomas and Stamnes. These calculations

generate look-up tables of cloud parameters. The LUTs are static and will be provided as ancillary data.

A general expression for the radiative transfer in the absence of thermal emission within the atmosphere can be formulated as:

$$\mu \frac{\mathrm{d}I(\mu,\varphi)}{\mathrm{d}\tau} = I(\mu,\varphi) - \frac{\omega_0}{4\pi} \int_0^{2\pi} \int_{-1}^{1} P(\mu,\varphi,\mu',\varphi') I(\mu',\varphi') \mathrm{d}\mu' \mathrm{d}\varphi' \qquad (10)$$

Measured attenuation of solar radiance is a function of the single scattering albedo ω_0, the scattering phase function P and the incoming solar radiation I. The reflected solar radiance at wavelength with no thermal emissions is a result of absorption and scattering processes within clouds and at the surface. Extinction in visible wavelengths is caused by scattering directly proportional to scattering cross-area. The size of cloud particles determines the shape of the scattering phase function and is therefore essential to retrieve the angular distribution of backscattered light. The amount of absorption in 3.75μm is directly proportional to the absorber volume. Extinction in absorbing channel is influenced by water absorption and thus, is a function of cloud particle size. The simultaneous retrieval of COD and CPS is required since scattering and absorption partition on extinction can otherwise not be separated.

Radiative transfer simulations have been performed to create a dataset as a basis for the forward calculations during the inversion process. They should cover the entire range of possible conditions and account for all parameters and processes, affecting the retrieval.

The RTM needs single scattering phase functions for water and ice droplets. Water particles were taken to be composed of spherical droplets at all wavelengths and Mie scattering ([*Wiscombe*, 1980]) was assumed for the inference of scattering and absorption properties.

For a given droplet size distribution and optical constants of water, a Mie-code returns extinction and scattering coefficients and the scattering phase function, which describes the angular distribution of scattered light in a single scattering event. The droplet size distribution is approximated by an analytical function, the modified Gamma-Hansen function

$$n(r) = r^{\frac{1-3r_b}{r_b}} e^{\frac{-r}{r_e r_b}} \qquad (11)$$

which is determined by two parameters: the effective radius r_e and a dispersion r_b about the effective radius. We assume for the dispersion (that is mean effective variance, a measure for the distribution width) a value of 0.1.

The RTM employs a delta-M scaling of the phase function. The model runs with a dataset on atmospheric temperature and cloud microphysical properties. Clouds are treated as plane parallel homogeneous layers of water, ice or liquid, droplets. The optical properties of the droplet size distribution are parameterized in terms of the effective radius.

A single-layered fast RTM is used for simulating the reflectance at the top of the atmosphere (TOA) for the ABI or AVHRR solar and near-infrared channels. The atmosphere in this model is divided into two cloud-free layers with a cloud layer between and a non-reflecting surface.

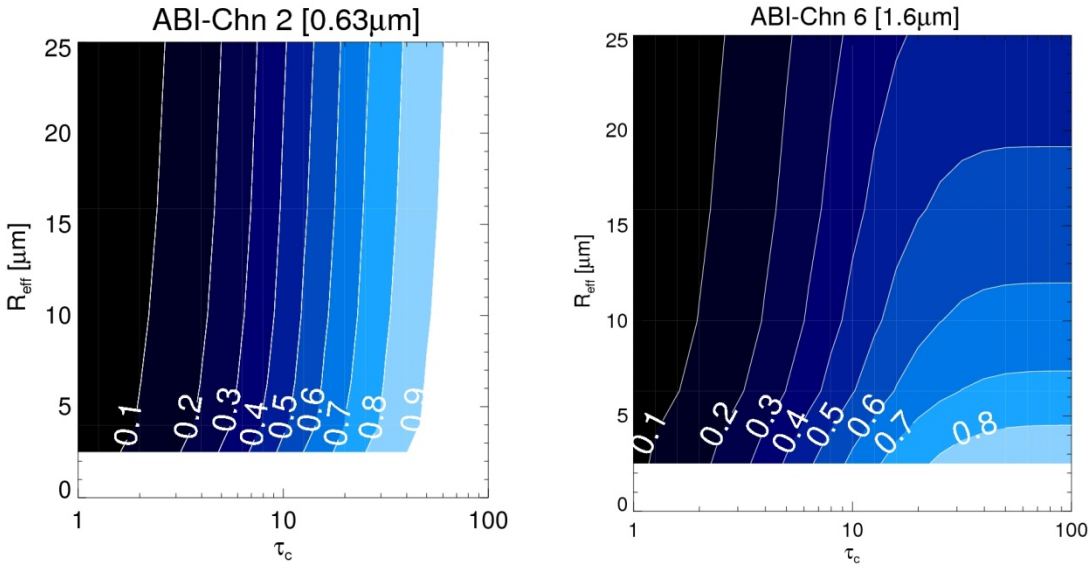

Figure 5. Example of simulated cloud reflectance as a function of optical depth and effective radius for ABI-channel 2 (left) and channel 5 (right). Satellite zenith is 20, Local zenith angle = 20 and Relative azimuth angle = 140.

Figure 5 illustrates that the reflectance in non-absorbing ABI channel 2 is primarily a function of cloud optical thickness. The reflectance is almost fully explained by the variations in optical depth, there is only weak sensitivity to effective radius. The right panel of Figure 5 shows that reflectance in Channel 6 is also highly sensitive to cloud optical thickness for thin clouds with $\tau_c < 10$. At thicker clouds this behavior changes to a higher sensitivity to effective radius.

The situation for ice clouds is more complex as the particles are generally not spherical. The assumption of spherical particle shapes for the ice phase leads to substantial

errors [*Mishchenko et al.*, 1996]. Ice clouds are currently composed of a mixture of habits consisting of droxtals (primarily for the smallest particles in a size distribution), hollow and solid columns, plates, 3D bullet rosettes, and aggregates. Current research activities are underway to implement 3D bullet rosettes with hollow bullets, which more closely approximate those observed in ice clouds. The hollow bullet rosettes also have very different scattering/absorption properties than those of solid bullet rosettes.

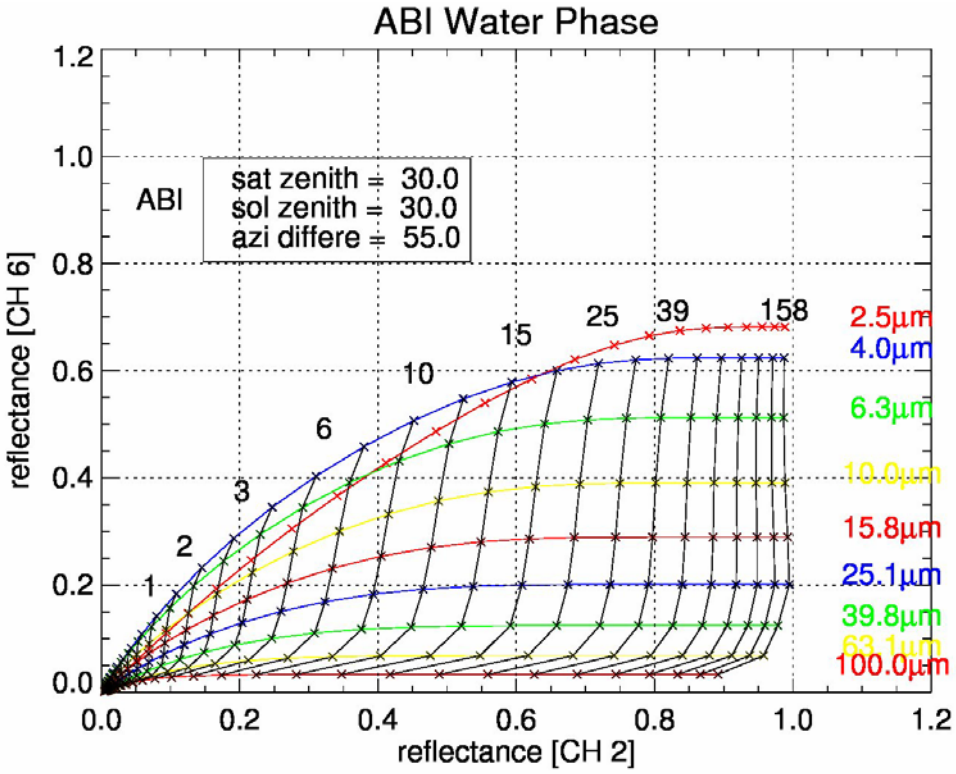

Figure 6. Theoretically computed cloud reflectance function for water phase of ABI channels 2 and 6 for an arbitrary geometrical observation constellation.

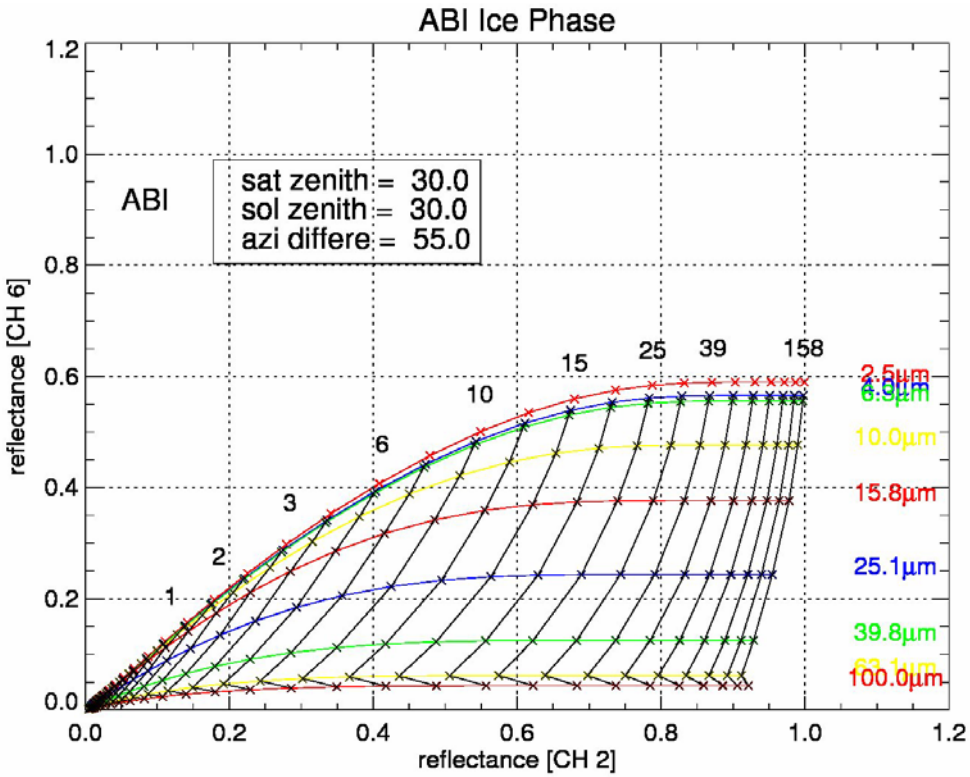

Figure 7. Same as Figure 6, but for ice clouds.

Figure 6 and Figure 7 show visualizations of the cloud reflectance function for an arbitrarily chosen observation geometry for ice and water clouds. Colored lines are the iso-lines of effective radius and black lines are the iso-lines of cloud optical depth. The line of equal 2.5 micron effective radius in the water cloud image crosses isolines of bigger particle distributions. The solution for measured reflectance values in this region is ambitious.

The following cloud parameters are extracted from the simulation output:

Cloud reflectance: The cloud reflectance R_C is a function of observation geometry and the cloud parameters τ_c and r_e. It denotes the bidirectional reflectance function of the cloud for light coming from above (i.e., the Sun). The RTM is able to calculate the radiative flux at any level in the atmosphere. The ratio between incoming and outgoing radiation at solar zenith, local zenith and azimuth angles denotes the cloud reflectance.

$$R_C(\tau_c, r_e, \theta_0, \theta, \Delta\phi) = \frac{\pi L\uparrow(\tau_c, r_e, \theta_0, \theta, \lambda)}{F_0(\lambda)\cos\theta_0} \qquad (12)$$

Cloud transmission: Cloud total transmission (diffuse plus direct) is calculated by computing the ratio of solar flux and the measured radiance below the cloud in the incoming path direction:

$$T_c(\tau_c, r_e, \theta_0) = \frac{\pi L\downarrow(\tau_c, r_e, \theta_0)}{F_0(\lambda)\cos\theta_0} \qquad (13)$$

Cloud albedo: Cloud albedo, also referred to plane albedo, depicts the overall backscattered radiance at a cloud level:

$$A_C(\tau, r_e, \mu_0) = \frac{1}{\pi}\int_0^{2\pi}\int_0^1 R_c(\tau, r_e, \mu, \mu_0, \Delta\phi) 2\mu_0 \mathrm{d}\mu \mathrm{d}(\Delta\phi) \qquad (14)$$

Cloud spherical albedo: Cloud spherical albedo is found by integrating the outgoing radiance over all azimuth angles as:

$$R_c^*(\tau_c, r_e) = \frac{2}{\pi}\int_0^1 \left[\int_0^{2\pi}\int_0^1 R_c(\tau_c, r_e, \mu, \mu_o, \Delta\varphi)\mu\, d\mu\, d(\Delta\varphi)\right] d\mu_o \qquad (15)$$

LUTs for both water and ice clouds that contain all cloud parameters described above for the relevant channels of all sensors were generated. The reflectivity LUTs are computed assuming a cloud above a non-reflecting (black) surface. With this simplified approach, there is no atmosphere and also no aerosols in the layers above and below the cloud layer. Nor is there multiple scattering between the cloud and a reflecting surface.

3.4.1.3 Impact of Surface Reflection

We consider the cloud as a single-layer homogeneously distributed cloud layer over a Lambertian surface having an albedo α_s. The calculations possess reflectance and transmittance functions given by $R_c(\tau_c, r_e, \mu_0, \mu, \Delta\phi)$ and $T_c(\tau_c, r_e, \mu_0)$, where μ is the cosine of the local zenith angle, μ_0 is the cosine of the solar zenith angle, and $\Delta\phi$ is the relative azimuth angle between the direction of propagation of the emerging radiation and the incident solar radiation, respectively. Tc denotes the diffuse and direct cloud transmittance for light from above, and T_c^* for light from below (following King, 1987). The total cloud-surface bidirectional reflectance function *R* at the top of the cloud (or atmosphere) can be expressed by:

$$R_{TOC} = R_c + \frac{A_{sfc}}{1 - A_{sfc} R_c^*} T_c T_c^* . \qquad (16)$$

Since R_c^* redirects downward the radiation from all incident angles, it is a directionally-integrated parameter; thus, it is only a function of τ_c and r_e. The value T_c is the cloud downward transmittance at the solar zenith angle μ_0. It is a hemispherical-integrated parameter and thus a function of optical thickness, effective particle size, and the solar zenith angle: $T_c = f(\tau_c, r_e, \mu_0)$. King (1987) discussed the use of reflected solar radiation measurements to infer τ_c. The surface albedo A_{sfc} is taken from MODIS white-sky albedo maps. If the snow mask detects snow or sea-ice a default value of 0.86 and 0.80 is used, respectively.

3.4.1.4 Interpolation

Within the LUTs the values will be searched with linear interpolation for all up to five dimensions. Standard models of linear interpolation are described in the following section.

We must first compute the following quantities with variables z, w, v representing the angular input variables (solar zenith, satellite zenith and relative azimuth difference) in case they are part of the LUT input for this simulation output.

For convenience and computational efficiency the individual LUTs are transformed in a smaller array with sub-arrays of all inputs:

$$\begin{aligned}
&R_c^{sub} = (r_{ijklm}) \subset R_C \\
&i = \{x_1; x_2\};\ j = \{y_1, y_2\}; k = \{w_1, w_2\}; l = \{v_1, v_2\}; m = \{z_1, z_2\} \\
&T_c^{sub} = (r_{ijk}) \subset T_C \\
&i = \{x_1; x_2\};\ j = \{y_1, y_2\}; k = \{w_1, w_2\} \\
&S^{sub} = (r_{ijk}) \subset S \\
&i = \{x_1; x_2\};\ j = \{y_1, y_2\}; k = \{w_1, w_2\}
\end{aligned} \qquad (17)$$

where x1,x2 are the next lower and upper LUT entrée index for the input value of the first dimension of the LUT. This is also set for the other dimensions with variables y, w, v, z. The quantities in the following describe the relative distance of the input value to the next LUT entrees for the respective dimension. . The methodology to calculate the weights used in the interpolation scheme ($q1$, $q2$, $q3$, $q4$, $q5$) are described in the "Get

Interpolation Weight Subroutine" section of the GOES-R AIADD. The values $p1$, $p2$, $p3$, $p4$, and $p5$ are simply 1 minus the interpolation weight (ex. $p1 = 1 - q1$).

3.4.1.5 Compute Partial Derivatives

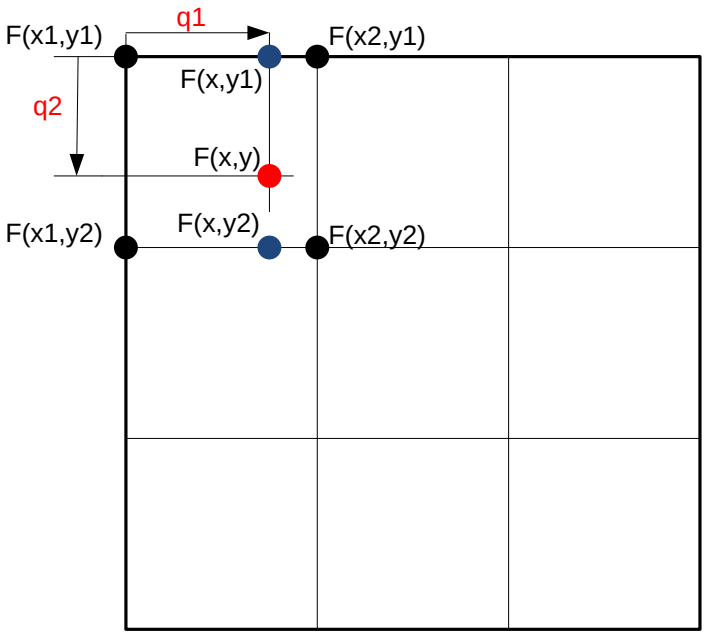

Figure 8. Pictorial depiction of LUT linear interpolation in both one and two dimensions.

This section is concerned with the numerical determination of the partial derivatives used to construct the Jacobian described used during the retrieval as described in section 3.4.1.8.

Partial derivatives in DCOMP are calculated in respect to τ_c or r_e from 2D fields of cloud reflectance, transmission or spherical albedo. Let now F(x,y) be any one of the functions above with the two variables $x = \tau_c$ and $y = r_e$. If we keep y constant with a value y_0 and differentiate f with respect to variable x, we obtain what is called the partial derivative of F with respect to x which is denoted by $\frac{\partial F(x, y_0)}{\partial x}$. Similarly if we keep x constant with a value x_0 and differentiate F with respect to the variable y, we obtain what is called the partial derivative of F(x,y) with respect to y which is denoted by $\frac{\partial F(x_0, y)}{\partial y}$. We can compute the partial derivatives of F referring to following:

$$
\begin{aligned}
F(x_1, y_0) &= p_2 F(x_1, y_1) + q_2 F(x_1, y_2) \\
F(x_2, y_0) &= p_2 F(x_2, y_1) + q_2 F(x_2, y_2) \\
\frac{\partial F(x, y_0)}{\partial x} &= \frac{F(x_2, y_0) - F(x_1, y_0)}{x_2 - x_1}
\end{aligned}
\qquad (18)
$$

Similarly for the derivatives in respect to y:

$$
\begin{aligned}
F(x_0, y_1) &= p_1 F(x_1, y_1) + q_1 F(x_2, y_1) \\
F(x_0, y_2) &= p_1 F(x_1, y_2) + q_1 F(x_2, y_2) \\
\frac{\partial F(x_0, y)}{\partial y} &= \frac{F(x_0, y_2) - F(x_0, y_1)}{y_2 - y_1}
\end{aligned}
\qquad (19)
$$

3.4.1.6 Atmospheric Correction

Atmospheric correction is needed to take into account any extinction processes in the atmospheric column. It will be carried out during the retrieval process at the pixel-level before the inversion process starts. A two-level atmospheric correction scheme is applied. First, the atmospheric transmittance above the cloud is determined. The radiative transfer can influence the observed signal at TOA in different ways. Extinction of the direct photon path leads to a reduction in the reflectance at the TOA signal. Scattering processes, which deflect photons into the observed path, increase the signal. The reflectance at TOC can be calculated as:

$$R_{TOC} = \frac{R_{TOA} - R_{sca}}{T_{ac}} \qquad (20)$$

R_{TOC}, R_{TOA} and R_{SCA} are the reflectance portions at TOC, TOA and the backscattered amount, respectively. The total transmission T_{ac} above the cloud ranges between 0 and 1. R_{TOC} is compared with the theoretical computed cloud reflectance R_C during the inversion process.

For the atmospheric layers below the cloud, the atmospheric transmission is considered by introducing a virtual surface albedo. The extinction below cloud expressed by T_{bc} can be treated as a reduction of the surface albedo:

$$A_{sfc,v} = A_{sfc} T_{bc} \qquad (21)$$

The virtual surface albedo $A_{sfc,v}$ substitutes the real surface albedo A_{sfc} for forward calculations. Non-negligible scattering processes occur only in the visible channel. Extinction is considered for scattering processes caused by air molecules (Rayleigh scattering) and aerosols and from absorption caused by water vapor, other trace gases, and ozone.

The transmission and backscattered reflection values under consideration of the relative amount of extinction in both channels are broken down as follows:

$$T_{ac,VIS} = T_r \; T_{aer} \; T_{o3} \; T_{h2o} \qquad (22)$$

$$T_{ac,NIR} = T_{h2o} \qquad (23)$$

We consider a backscattered signal R_{sca} only in the visible channel from Rayleigh scattering, so that

$$R_{sca,VIS} = R_{sca,r} \qquad (24)$$

$$R_{sca,NIR} = 0 \qquad (25)$$

The following subsections explain the individual parts of atmospheric correction in detail.

3.4.1.6.1 Atmospheric Correction for Rayleigh scattering

Rayleigh scattering has a primary impact in the visible channel. Scattering in the near-infrared channel at 2.2 μm is weak and negligible and is therefore ignored in the DCOMP algorithm. The potential error especially for thin clouds or high observing and solar angles reaches values from more than 10%. Figure 9 depicts the importance of Rayleigh correction for cloud optical depth retrieval.

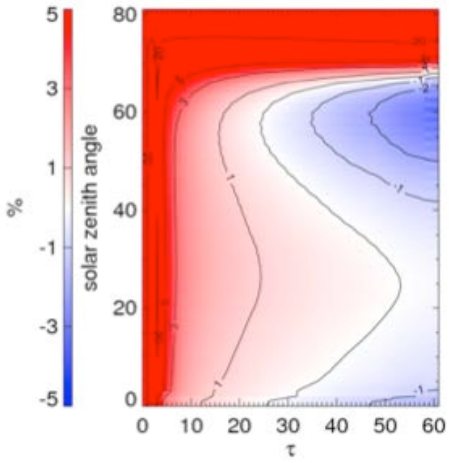

Figure 9. Potential error in percent if Rayleigh correction is not applied as a function of τ_c and solar zenith angle. Observation angle is 43 degrees and effective radius is 8 μm.

The correction scheme mainly follows the correction scheme by [*Wang and King*, 1997], which was also applied to MODIS processing. We consider the full atmospheric column of Rayleigh optical depth as $\tau_{r,0} = 0.044$. The resulting Rayleigh optical depth above the cloud is calculated by

$$\tau_r = \tau_{r,0}\left(\frac{p_c}{p_{sfc}}\right) \quad (26)$$

where p_c denotes the cloud top pressure provided by the ABI Cloud Height algorithm and p_{sfc} denotes the surface pressure and is provided by the NWP dataset.

It was assumed that the upward radiance at TOA can be broken down into four components by a single scattering assumption:

i. direct molecular scattering without reflection from the cloud;

ii. single scattering in the air toward the cloud followed by reflection from the cloud;

iii. as (ii), but vice versa; and

iv. direct reflection of the solar beam from the cloud.

[*Wang and King*, 1997] stated that under the single scattering assumption, the signal at the sensor R_{TOA} is composed of four parts by using cloud albedo A_c, the Rayleigh phase function P_r:

$$R^{(i)}(\tau_r,\theta,\theta_0,\Delta\phi)=\frac{\tau_r P_r(\theta,\theta_0,\Delta\phi)}{4\mu\mu_0} \quad (27)$$

$$R^{(ii)}(\tau_r,\tau_c,r_e,\theta,\theta_0)=\frac{\tau_r}{2\mu_0}A_C(\tau_C,r_e,\theta)e^{-\tau_r/\mu} \quad (28)$$

$$R^{(iii)}(\tau_r,\tau_c,r_e,\theta,\theta_0)=\frac{\tau_r}{2\mu}A_C(\tau_C,r_e,\theta_0)e^{-\tau_r/\mu_0} \quad (29)$$

$$R^{(iv)}(\tau_r,\tau_c,r_e,\theta,\theta_0,\Delta\phi)=R_{TOC}(\tau_c,r_e,\theta,\theta_0,\Delta\phi)e^{[-\tau_r AMF]} \quad (30)$$

$$R_{TOA}=R^{(i)}+R^{(ii)}+R^{(iii)}+R^{(iv)} \quad (31)$$

where $AMF=\frac{1}{\cos\theta}+\frac{1}{\cos\theta_0}$ is air mass factor. The four parts are the direct scattering at an air molecule without reflection from the cloud ($R^{(i)}$), a scattering first at an air molecule with a subsequent reflection at the cloud ($R^{(ii)}$), the reflection first at the cloud top with a subsequent scattering event at an air molecule ($R^{(iii)}$), and the direct reflection at the cloud top ($R^{(iv)}$)

We assume a Rayleigh optical depth for an atmospheric column from the surface to TOA for the visible channel of $\tau_{r0}=0.044$. Rayleigh optical depth above the cloud are estimated by

$$\tau_r=\frac{p_c}{p_{sfc}}\tau_{r0} \quad (32)$$

where p_{sfc} and p_c are the surface pressure and the pressure at the cloud top, respectively. We use an NWP re-analysis surface pressure for p_{sfc} and ACHA cloud top pressure for p_c. The Rayleigh phase function is expressed by

$$P_r(\theta,\theta_0,\Delta\phi)=\frac{3}{4}(1+\cos\zeta(\theta,\theta_0,\Delta\phi)^2) \quad (33)$$

where $\zeta(\theta,\theta_0,\Delta\phi)$ is the scattering angle.

The cloud albedo function A_c is given as pre-calculated LUTs as a function of τ_c, r_e, θ_0. Thus, the Rayleigh atmospheric correction should be a part of the optimization process for a perfect solution. However, the potential error is low and the computational cost would be immense if the Rayleigh correction would be a part of the inversion. Thus, to simplify the retrieval we approximate the effective radius r_e to be $10\mu m$ for water clouds and approximately $20\mu m$ for ice clouds. The residual problem turns to a 1D problem and the corresponding cloud optical depth can be found now by searching the minima difference between the observation in the visible channel and the LUT values for the visible channel for the chosen effective radius.

The term $e^{-\tau_r AMF}$ is the total two-way Rayleigh transmission function T_{ac} of the photon path on its way from the top of the atmosphere to the cloud surface and back to the sensor. Now we can formulate a Rayleigh specific version of the equation.

$$R_{TOC} = \frac{R_{TOA} - (R^{(I)} + R^{(II)} + R^{(III)})}{T_{ac}} \qquad (34)$$

The values to include are as follows:

$$T_{r,VIS} = e^{-\tau_r AMF} \qquad (35)$$

$$T_{r,NIR} = 1. \qquad (36)$$

$$R_{sca,VIS} = R^{(I)} + R^{(II)} + R^{(III)} \qquad (37)$$

3.4.1.6.2 Atmospheric Correction for Aerosol Scattering Effects

For atmospheric correction of aerosols above clouds we assume a background aerosol optical depth of $\tau_{aer;0}$= 0.1 with an asymmetry parameter g assumed to equal 0.6. The expression for the aerosol optical depth above a cloud takes into account the assumed vertical distribution of aerosol in the atmosphere with

$$\tau_{aer} = \left(\frac{p_c}{p_{sfc}} \right)^4 \tau_{aer,0} \qquad (38)$$

Forward scattering dominates the aerosol phase function of the aerosol. Thus, it is appropriate to substitute the optical depth by the scaled optical depth as:

$$\tau'_{aer} = \tau_{aer}(1-\omega_0 g) \qquad (39)$$

Background full-path aerosol parameters are summarized in Table 7.

Table 7 Global settings for aerosol parameters

Parameter	Symbol	Value
Aerosol optical depth	τ_{aer}	0.1
Single-scattering albedo	ω_0	0.9
Asymmetry	g	0.6

The relevant parameter for the correction scheme is:

$$T_{aer,VIS} = e^{-\tau'_{aer} AMF} \qquad (40)$$

We assume transmission in the infrared channel as 1 and the backscattered portion as insignificant.

With the considerations for Rayleigh and aerosol atmospheric correction we can define an effective phase functions for scattering processes as:

$$P_{eff}(q) = \frac{w_{0,aer} t_{aer} P_{aer}(q) + t_{ray} P_{ray}(q)}{t_{tot}} \qquad (41)$$

3.4.1.6.3 Atmospheric Corrections for Water Vapor Absorption and Trace Gases

To simplify the atmospheric corrections, the transmission of gas is parameterized as an analytical function of the effective absorber amount.

Water vapor mass above and below cloud is obtained from NWP water vapor profiles. The ACHA cloud top height is used for determining the cloud top level. The input profiles are functions of water vapor amount above the respective level w = f(z):

$$u_{h_2o}^{AC}(cth) = w(cth) \qquad (42)$$

The water vapor mass below cloud is calculated by the difference between the full column water vapor and the amount above the cloud top height as.

$$u_{h_2o}^{BC} = w(cth = 0) - u_{h_2o}^{AC} \qquad (43)$$

In case of invalid NWP water profile data, u is set to a minimal value of 0, if this value becomes negative for corrupt data. Water vapor transmission is a function of the water vapor mass. MODTRAN simulations are used to find coefficients $c_{0,1,2}$ which are applied to find the optical depth of water vapor according to:

$$\tau_{h_2o,\lambda} = c_{0,\lambda} + c_{1,\lambda} u_{h_2o} + c_{2,\lambda} u_{h_2o}^2 \qquad (44)$$

where u_{h_2o} is water vapor column in mm column amount.

The transmission is now computed by:

$$T_{h_2o} = e^{-AMF\,\tau_{h_2o}} \qquad (45)$$

where AMF is the relative air mass for both ways from the top of atmosphere and back, $\tau_{H_2O,\lambda}$ is the optical depth of water vapor for a certain wavelength, c are coefficients retrieved by MODTRAN and W is the water vapor amount above the cloud.

Table 8 Atmospheric correction coefficients

		a_0	a_1	a_2
MODIS	0.6 H_2O	−0.000 393 77	0.004 104 35	−0.000 126 045
	1.6 H_2O	−0.000 190 805	0.001 038 88	-1.7948×10^{-5}
	3.8 H_2O	0.010 512 8	0.050 244 5	−0.002 541 75
	0.6 O_3	0.010 512 8	$8.919\,293\,2 \times 10^{-5}$	$-1.904\,334 \times 10^{-8}$
NOAA-18	0.6 H_2O	0.000 096 04	0.003 515 63	−0.000 102 50
	1.6 H_2O	−0.000 166 318	0.001 104 78	$-1.957\,17 \times 10^{-5}$
	3.9 H_2O	0.012 701 0	0.049 214 1	−0.002 383 03
	0.6 O_3	−0.001 48	−0.000 106 56	$-2.303\,879 \times 10^{-8}$
GOES-13	0.6 H_2O	0.000 320 90	0.004 550 23	−0.000 165 50
	3.9 H_2O	0.005 247 30	0.023 630 9	−0.001 137 38
	0.6 O_3	−0.000 518 4	$9.341\,763\,6 \times 10^{-5}$	$-7.631\,08 \times 10^{-9}$
SEVIRI	0.6 H_2O	0.000 102 2	0.002 454 72	$-5.544\,08 \times 10^{-5}$
	1.6 H_2O	0.007 239 54	0.002 979 67	$-5.659\,69 \times 10^{-5}$
	3.9 H_2O	0.006 794 56	0.029 710 0	−0.001 569 44
	0.6 O_3	0.000 176 8	$9.140\,529 \times 10^{-5}$	$5.450\,645\,3 \times 10^{-9}$

Table 8 includes the coefficients for MODIS, AVHRR, ABI and the proxy sensor.

Figure 10 shows the transmission for AMF =1 as a function of the absorber mass for both channels.

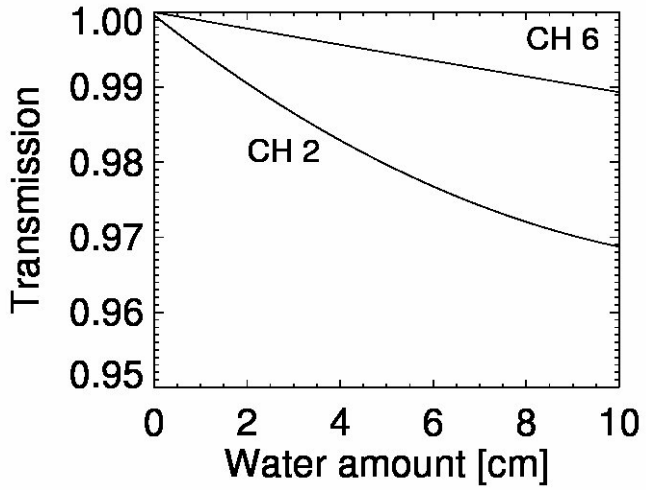

Figure 10. Water vapor transmission as a function of absorber amount.

3.4.1.7 Ozone

Similarly, ozone transmission is calculated as:

$$T_{o_3} = e^{-AMF\,\tau_{o_3}} \qquad (46)$$

where τ_{o_3} is the ozone optical thickness;

$$\tau_{o_3} = c_0^{o_3} + c_1^{o_3} u_{o_3} + c_2^{o_3} u_{o_3}^2 \qquad (47)$$

The value u_{o_3} is the ozone absorber mass in Dobson units. The coefficients were computed by MODTRAN simulations. Values are given in Table 8. Ozone transmission is ignored in the near infrared channel.

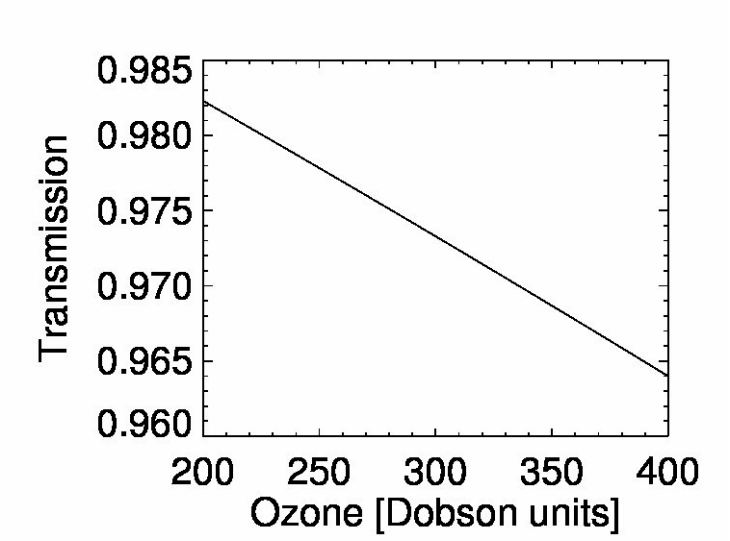

Figure 11. Ozone transmission as a function of absorber amount

3.4.1.8 Optimal Estimation Inversion Technique

Using optimal estimation (OE) proved to be a fast and accurate inversion technique for deriving properties from satellite measurements [Rodgers, 2000] . This OE-algorithm aims to minimize a cost-function accounting for measurement errors, and prior knowledge given by simple assumptions.

The covariance error matrix of the state x is calculated by

$$\mathbf{S_x} = (\mathbf{S_a^{-1}} + \mathbf{K^T S_y^{-1} K})^{-1} \qquad (48)$$

where y is the observation vector, x the state vector, $\mathbf{x}_a$ the a-priori state vector, F the forward model operator, K the Kernel and $\mathbf{S}_a$ and $\mathbf{S}_y$ the observation and background error covariance matrixes. The setting of the prior knowledge parameters $\mathbf{x}_a, \mathbf{S}_a$ and $\mathbf{S}_y$ are explained in the next section. The state vector x for the next iteration step $i+1$ is calculated after a row of iterative steps according to

$$\mathbf{x}_{i+1} = \mathbf{x}_i + \delta\mathbf{x} \qquad (49)$$

$$\delta\mathbf{x} = \mathbf{S_x}\left(\mathbf{K^T S_y^{-1}}(\mathbf{y} - \mathbf{F}(\mathbf{x}_i)) + \mathbf{S_a^{-1}}(\mathbf{x_a} - \mathbf{x})\right) \qquad (50)$$

Starting from a first guess that is typically the a priori value $\mathbf{x}_a$, the iteration is performed until a convergence criterion is fulfilled or the number of iterations exceeds a maximum threshold. The convergence test in DCOMP is based on the size of the iteration step in the state space. The retrieval iterations are conducted until the following criterion is met:

$$d_i^2(\mathbf{x}_i - \mathbf{x}_{i+1}) = (\mathbf{x}_i - \mathbf{x}_{i+1})^T \mathbf{S}_x^{-1}(\mathbf{x}_i - \mathbf{x}_{i+1}) \le \frac{p}{2} \qquad (51)$$

where p is the number of elements of x (p = 2).

In DCOMP the y and x vectors are defined as follows.

$$\mathbf{x} = \begin{pmatrix} \tau \\ r_e \end{pmatrix} \qquad (52)$$

$$\mathbf{y} = \begin{pmatrix} R_{VIS} \\ R_{IR} \end{pmatrix} \qquad (53)$$

The Kernel matrix K contains the partial derivatives of each element of $F(x)$ in respect to each element of x.

$$\mathbf{K} = \begin{pmatrix} \frac{\partial R^{ch2}}{\partial \tau} & \frac{\partial R^{ch2}}{\partial r_e} \\ \frac{\partial R^{ch6}}{\partial \tau} & \frac{\partial R^{ch6}}{\partial r_e} \end{pmatrix} \quad (54)$$

The forward operator, which accounts for the surface is calculated by:

$$\mathbf{F}(\mathbf{x}) = R_c(\mathbf{x}, \theta, \theta_0, \Delta\varphi) + \frac{A_{sfc}}{1 - A_{sfc} R_C^*(\mathbf{x})} T(\mathbf{x}, \theta) T(\mathbf{x}, \theta_0) \quad (55)$$

The cloud reflectance R_C, spherical albedo R_C^* and the transmission T are determined from the LUTs. The surface albedo is given by the MODIS white sky albedo ancillary dataset. The individual components of $\mathbf{F}(\mathbf{x})$ are:

$$R^{ch2} = R_c^{ch2}(\mathbf{x}, \theta, \theta_0, \Delta\varphi) + \frac{A_{sfc}^{ch2}}{1 - A_{sfc}^{ch2} R_C^{*,ch2}(\mathbf{x})} T^{ch2}(\mathbf{x}, \theta) T^{ch2}(\mathbf{x}, \theta_0) \quad (56)$$

$$R^{ch6} = R_c^{ch6}(\mathbf{x}, \theta, \theta_0, \Delta\varphi) + \frac{A_{sfc}^{ch6}}{1 - A_{sfc}^{ch6} R_C^{*,ch6}(\mathbf{x})} T^{ch6}(\mathbf{x}, \theta) T^{ch6}(\mathbf{x}, \theta_0) \quad (57)$$

For better readability in the subsequent equations we substitute the second term of the above equations with :

$$D_{sfc} = \frac{A_{sfc}^k}{1 - A_{sfc}^k R_C^{*,k}(\mathbf{x})} \quad (58)$$

The components of $\mathbf{K}$ are derivatives of each forward model with respect to the components of the state vector and are calculated by:

$$\frac{\partial R^k}{\partial \tau} = \frac{\partial R_c^k}{\partial \tau} + D_{sfc} T^{ch6}(\mathbf{x},\theta) \frac{\partial T^k(\mathbf{x},\theta_0)}{\partial \tau} + D_{sfc} \frac{\partial T^k(\mathbf{x},\theta)}{\partial \tau} T^k(\mathbf{x},\theta_0) + \frac{\partial D_{sfc}}{\partial \tau} T^{ch6}(\mathbf{x},\theta) T^k(\mathbf{x},\theta_0) \quad (59)$$

where k denotes the channel number 2 or 6 and derivatives of D_{sfc} are calculated by:

$$\frac{\partial D_{sfc}^k}{\partial \tau} = \frac{A_{sfc}^k A_{sfc}^k \frac{\partial R_c^{*,k}}{\partial \tau}}{(1 - A_{sfc}^k R_c^{*,k})^2} \quad (60)$$

Similar for the derivative to the effective radius:

$$\frac{\partial R^k}{\partial r_e} = \frac{\partial R_c^k}{\partial r_e} + D_{sfc}^k T^k(\mathbf{x},\theta) \frac{\partial T^k(\mathbf{x},\theta_0)}{\partial r_e} + D_{sfc}^k \frac{\partial T^k(\mathbf{x},\theta)}{\partial r_e} T^k(\mathbf{x},\theta_0) + \frac{\partial D_{sfc}^k}{\partial r_e} T^k(\mathbf{x},\theta) T^k(\mathbf{x},\theta_0) \quad (61)$$

with

$$\frac{\partial D_{sfc}^k}{\partial r_e} = \frac{A_{sfc}^k A_{sfc}^k \frac{\partial R_c^{*,k}}{\partial r_e}}{(1 - A_{sfc}^k R_c^{*,k})^2} \quad (62)$$

The maximum iteration number is set to 22. It can be shown that for the bulk of the pixels, the algorithm converges after 5-8 iterations. If the inversion loop exceeds iteration number of 20, it is very unlikely that a valid result is achievable.

3.4.1.9 Estimation of Prior Values and their Uncertainty

The proper implementation of DCOMP requires meaningful estimates of a priori values housed in $\mathbf{x_a}$ and their uncertainties housed in $\mathbf{S_a}$. For DCOMP, we assume $\mathbf{S_a}$ is a diagonal matrix with each element assumed to be the variance of each element of $\mathbf{x_a}$ as illustrated below:

$$S_a = \begin{pmatrix} \sigma^2_{\tau,ap} & 0 \\ 0 & \sigma^2_{r_e,ap} \end{pmatrix} \qquad (63)$$

Since almost all estimates of COD and CPS from other algorithms are based on similar approaches, there is no robust a priori for these cloud parameters. In general, it is assumed that water clouds have a maxima effective radius size of up to 30 microns with an average of about 10 microns. Ice particles may have effective radii of up to 100 microns with a higher average. Optical depth is directly related to the extinction by scattering in a conservative wavelength. Consequently, we selected a priori value that is related to the reflectance in the visible channel and the a priori value of the effective radius. We search for the point of the iso-line of the a priori effective radius, where the observed reflectance in the visible channel is true, and take the corresponding optical depth as the a priori value.

According to the findings of several publications, we set the following a priori values for water:

$$\mathbf{x_{ap}} = \begin{pmatrix} \tau_{ap} \\ r_{e,ap} \end{pmatrix} = \begin{pmatrix} f(10, R_{CH2}) \\ 10^1 \mu m \end{pmatrix} \qquad (64)$$

and for ice:

$$\mathbf{x_{ap}} = \begin{pmatrix} \tau_{ap} \\ r_{e,ap} \end{pmatrix} = \begin{pmatrix} f(10^{1.3} \mu m, R_{CH2}) \\ 10^{1.3} \mu m \end{pmatrix} \qquad (65)$$

The uncertainty of these assumptions is high. Thus, we set the values $\sigma_{\tau,ap}$ and $\sigma_{r_e,ap}$ to 0.2 or the a priori value of τ, and 0.5 for water and 0.75 for ice.

3.4.1.10 Estimation of Forward Model Uncertainty

This section describes the estimation of the elements of $\mathbf{S_y}$ which contain the uncertainty of the observation vector $\mathbf{y}$ as a variance of the forward model estimates. As was the case with $\mathbf{S}_a$, $\mathbf{S_y}$ is assumed be a diagonal matrix.

Assumed to be diagonal, $\mathbf{S}_y$ can be expressed as follows.

$$S_y = \begin{pmatrix} \sigma^2_{CH2,ap} & 0 \\ 0 & \sigma^2_{CH6,ap} \end{pmatrix} \qquad (66)$$

The variance terms are computed by summing up three components:

$$\sigma = \sigma_{OFF} + R^k(\sigma_{clb} + \sigma_{fm} + \sigma_{pp}\sigma_{hetero}) \qquad (67)$$

The first component gives an offset as a bottom value for the assumed error. The sum of calibration error σ_{clb}, forward model error σ_{fm} and the plan-parallel error σ_{pp}multiplied by a measure of spatial heterogeneity $\sigma_{hetero}$is weighted by the measured reflectance R^k of the individual channels k. The last term can be seen as an estimate of the error, which would occur if the plan-parallel assumption fails. We assume that this is particular uncertain in case of low spatial homogeneity.

If the snow mask from the framework detects snow surfaces, we will give the observations in the visible channel very low trust. This fact is reflected in a high value for σ in the visible channel.

Table 9 The error estimated in forward model uncertainty in DCOMP

		Channel 2	**Channel 6**
Calibration error	σ_{clb}	0.05	0.05
Forward model error water	σ_{fm}	0.01	0.01
Forward model error ice	σ_{fm}	0.03	0.03
Plan parallel error	σ_{pp}	0.1	0.1
Offset value	σ_{off}	0.02	0.02
Snow exception	σ_{snow}	1000.	

3.4.2 Data Merging Strategy

Not Applicable

3.4.3 Numerical Strategy

An adequate transformation scheme is established to transform the radiance measurements into reflectivity quantities by considering the geometrical constellation.

A doubling/adding radiative transfer model (RTM) is used to solve the forward problem, i.e., the derivation of satellite sensor signals (radiance) by simulating the transfer of solar radiation through the atmosphere for given cloud parameters. Additionally, the RTM calculates transmittance and spherical albedo of a cloud layer. Inferring the optical properties from measured satellite radiances is called the inverse problem. This problem will be managed by a 1D-var optimal estimation approach. A priori assumptions and covariance matrices depend on prior knowledge of climate data sets.

Applying a radiative transfer model to quantify the influence of the cloud microphysical parameters on the backscattered solar radiation measured at the sensor.

Generating look-up-tables (LUT) for cloud reflectivity of one channel in visible spectrum at 0.6 μm and for one near-infrared channel at 1.6, 2.2, or 3.75 μm for a wide range of possible sun/sensor geometry constellations.

Receiving from the processing framework all other derived (cloud mask, cloud height, and cloud phase) and ancillary data needed by the COD/CPS algorithms.

Using 1D-var optimal estimation inversion techniques to retrieve the optical thickness and particle size from LUTs of channel reflectivity based on optimal estimation method.

3.4.4 Calculations

Not Applicable.

3.4.5 Look-Up Table Description

The LUTs are generated both for water and ice clouds. The following central wavelength lookup tables will be provided for water and ice clouds:

1. 0.64 μm
2. 1.61 μm
3. 2.20 μm
4. 3.75 μm

The following parameters have been included in the lookup table sets.

For water clouds the following set-up is determined:

1. 45 Solar zenith angles: 0 to 88 degrees in steps of 2 degrees.
2. 45 Local zenith angles: 0 to 88 degrees in steps of 2 degrees.
3. 45 Azimuth angle difference: 0 to 170 degrees in steps of 5 degrees
4. 170 to 180 degrees in steps of 1 degree
5. 9 Effective radii: defined in log10 space → 0.4 to 2.0 in steps of 0.2
6. 29 Cloud optical depths: defined in log10 space → -0.6 to 2.2 in steps of 0.1

The set-up for ice clouds is defined as:

1. 45 Solar zenith angles: 0 to 88 degrees in steps of 2 degrees.
2. 45 Local zenith angles: 0 to 88 degrees in steps of 2 degrees.
3. 45 Azimuth angle difference: 0 to 170 degrees in steps of 5 degrees
4. 170 to 180 degrees in steps of 1 degree
5. 9 Effective radii: defined in log10 space → 0.4 to 2.0 in steps of 0.2
6. 29 Cloud optical depths: defined in log10 space → -0.6 to 2.2 in steps of 0.1

LUTs are calculated for the

1. Cloud reflectivity function calculated for a non-reflective surface (albedo = 0) as a function of cloud optical depth, effective radius, solar zenith , local zenith and relative azimuth angle difference with a dimension of [45,45,45,9,29];
2. Cloud transmission function as function of cloud optical depth and effective radius and solar zenith angle (dimension [45,9,29]);
3. Spherical albedo as a function of cloud optical depth and effective radius ([9,29]); and
4. Cloud albedo as a function of cloud optical depth and effective radius and incoming angle (9,29,45).

3.4.6 Parameterization

Not Applicable

3.4.7 Algorithm Output

3.4.7.1 Output

The data product includes two float-typed datasets for cloud optical depth and cloud effective radius. The product data type is HDF-4 formatted file.

Note, that an output for each pixel is either liquid water path or ice water path.

Table 10 Algorithm output

Name	Type	Description	Dimension	Unit
COD	output	Cloud optical depth	grid (xsize, ysize)	without
REF	output	Cloud effective radius	grid (xsize, ysize)	μm
LWP	output	Liquid water path	grid (xsize, ysize)	g/m2
IWP	output	Ice water path	grid (xsize, ysize)	g/m2
QC flags	output	Quality control flags for each pixel	grid (xsize, ysize)	without

3.4.7.2 Quality Flags

In addition to the algorithm output, a pixel level quality flag will be assigned. Since all products are generated in parallel, we set one single level of quality flags for DCOMP instead of one quality for each product. The possible values are as follows:

Table 11 Quality Flags in DCOMP output

Flag Value	Description
0	Valid, good quality converged retrieval
1	Not valid, quality may be degraded due to snow or sea ice surface
2	Not valid, degraded quality due to twilight conditions (solar zenith between 65 and 82 degree)
3	Invalid due to cloud-free condition
4	Invalid pixel due to being outside of observation range
5	Invalid pixel due to missing input data
6	Invalid pixel, DCOMP attempted but failed retrieval

A full quality pixel quality flag will set a flag value = 0. Snow and surface pixel may degrade the quality of the products. The quality flag is then set to 1. Twilight pixels

with assumed degraded quality are set to 2. Cloud-free pixels are set to 3. If a pixel is outside the observation limits for solar zenith angle, local zenith angle, or look into space, the quality flag is set to 4. If any needed input data are missing, such as cloud mask, cloud top pressure, any CFSR data or surface albedo, the value is set to 5. If DCOMP could start, but the retrieval failed to converge, the QF is set to 6.

3.4.7.3 Processing Information Flag

In addition to the algorithm output and quality flags, processing information, or how the algorithm was processed, will be output for each pixel. If the bit is 0, then the answer was no, and if the bit is 1, the answer is yes.

Table 12 Processing Information Flags in DCOMP

Bit	Description
0*	Invalid due invalid observation geometry?
1*	Invalid due to being cloud-free or probably cloud-free?
2*	Invalid due to missing ancillary data?
3	Sea pixel?
4	Snow pixel?
5	Sea-ice pixel?
6	Use of default surface albedo if MODIS white-sky albedo is missing?
7	Optimal Estimation attempted, but retrieval failed
8	Retrieval successful

*If these bits are set, the retrieval is interrupted for this pixel and all following bits are not set.

3.4.7.4 Metadata

The output files will include the following metadata:

- Day/Night flag
- Mean, Min, Max and standard deviation of cloud optical depth
- Mean, Min, Max and standard deviation of cloud particle size
- Number of QA flag values
- For each QA flag value, the following information is required:
- Number of retrievals with the QA flag value

- Definition of QA flag
- Total number of detected cloud pixels
- Terminator mark or determination

4. Test Datasets and Outputs

4.1 Test Input Datasets

The primarily test data source for developing and testing DCOMP algorithm are SEVIRI observations. SEVIRI provides similar channel settings, except for the 2.2 μm channel, compared to GOES ABI and is therefore well suited to be the testbed of any GOES ABI algorithm. In the development phase we used SEVIRI's 1.6 μm channel, which is similar to GOES ABI channel 5.

Table 13 Comparison of AVHRR, SEVIRI and ABI channels.

Sensor	Channel No.	Wavelength Center (μm)	Band width (μm)	Spatial Resolution (km)
AVHRR	1	0.63	0.58 – 0.68	1.09
	3b	3.75	3.55-3.93	1.09
ABI	2	0.64	0.59 – 0.69	0.5
	6	2.25	2.225-2.275	1
SEVIRI	1	0.64	0.56 – 0.71	3-5
	3	1.64	1.50 – 1.78	3-5

SEVIRI provides 11 spectral channels with a spatial resolution of 3-5 km and a temporal resolution of 15 minutes. SEVIRI provides the best source of data currently for testing and developing GOES-R products. Figure 12 shows a full-disk RGB composite of a SEVIRI scene from 13 UTC on August 1, 2006. The SEVIRI data were provided by the SSEC Data Center.

Note that due to differences in central wavelength and spectral response function, radiative transfer simulations and generated look-up-tables are different. The SEVIRI spectral response functions were obtained by EUMETSAT.

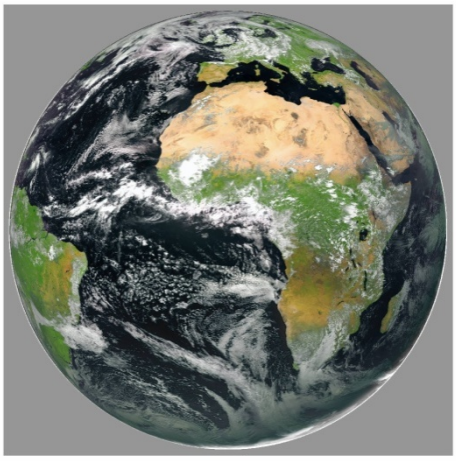

Figure 12. Full disk false color image from SEVIRI 13UTC on 1 August 2006.

The DCOMP source code can be directly applied to SEVIRI input data. Except for the exact channel settings, all components of the algorithm system, such as radiative transfer model, LUT design and inversion techniques are identical.

The look-up-tables for cloud characterization parameters and atmospheric correction factors are provided separately for AVHRR and GOES-ABI and the proxy data set due to different response functions. The software uses information from algorithm input files and assigns the correct LUTs.

4.2 Test Output Analysis

4.2.1 Reproducibility

Figure 13 shows DCOMP products from SEVIRI observations for 13:00 UTC on 1 August 2006. During both the TRR and subsequent tests, comparisons between the online (Framework) and offline (Cloud AWG) output of DCOMP, when the same inputs were used, showed an exact match of the results.

The images in Figure 13 illustrate the DCOMP cloud optical depth, Cloud Particle Size, Liquid Water Path and Ice Water Path. These images correspond to 13 Z on 1 August 2006 and correspond to the RGB image above. This day and scene was chosen since it was also used in a EUMETSAT SEVIRI cloud product comparison workshop in Locarno/Switzerland.

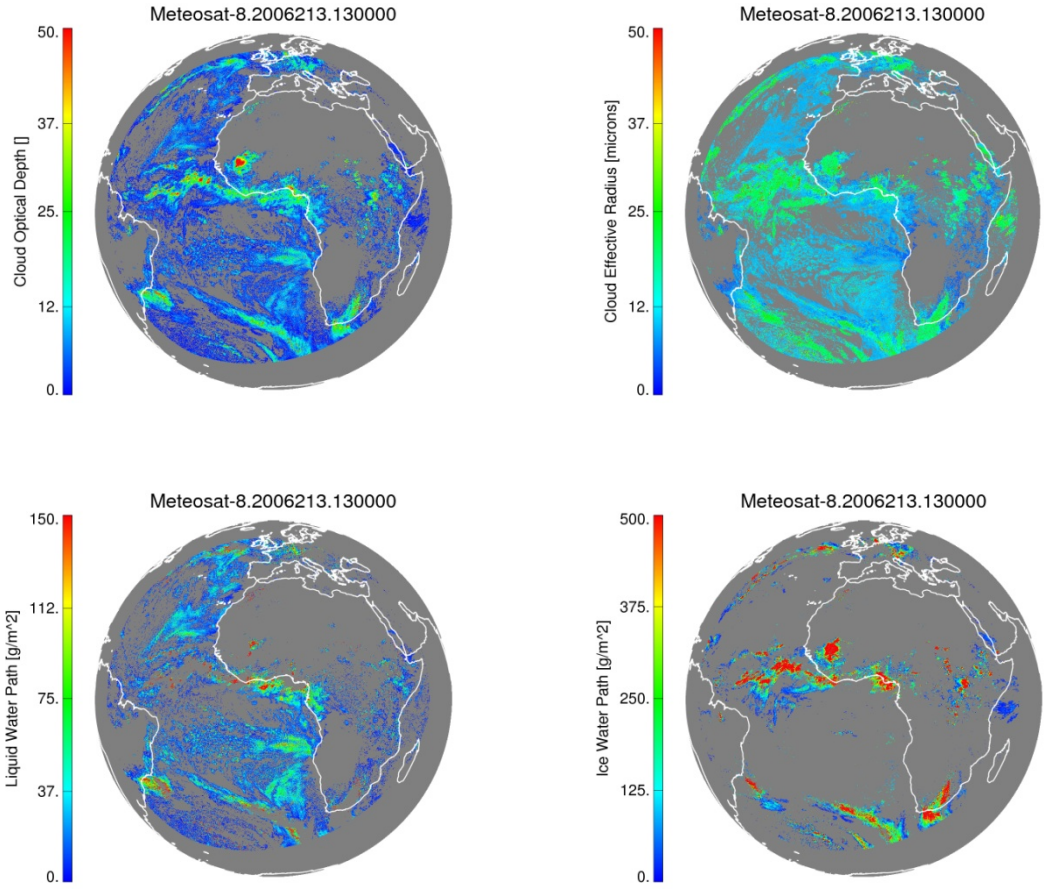

Figure 13. Results of the retrieval for 1 August 2006 13:00UTC for SEVIRI. Upper panel shows optical depth (left) and effective radius (right). Lower panel shows liquid water path (left) and ice water path (right).

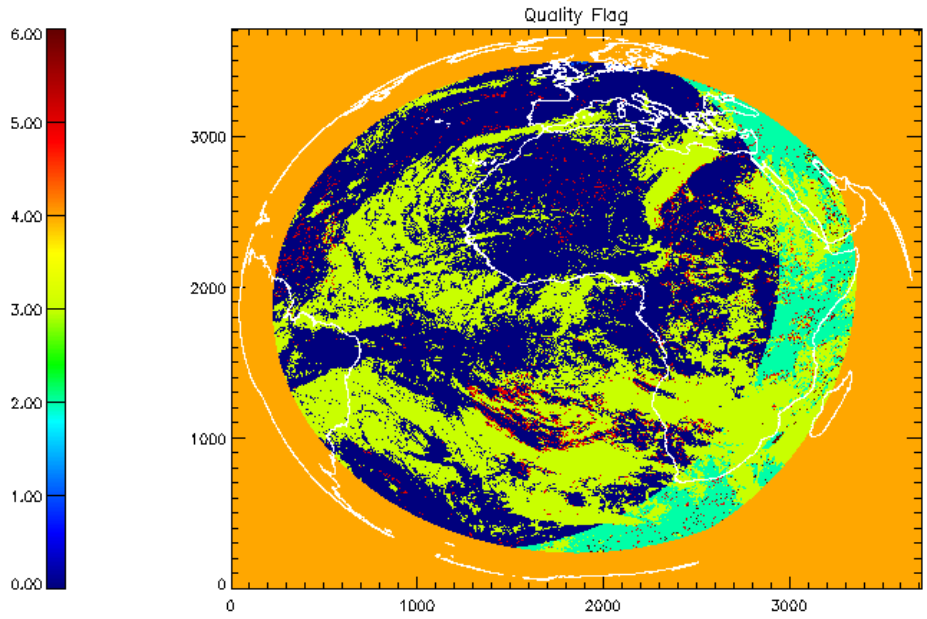

Figure 14. Example for Quality Flag information for SEVIRI scene on day 238 at 12 Z in 2006.

An example for quality flag output is shown in Figure 14. Blue pixels indicate successful retrieval with full quality. The green areas have retrieved values but with degraded quality since the solar zenith angles are above 65 degrees. Yellow pixels are cloud-free pixels. The isolated red pixels are examples of failed retrievals.

4.2.2 Precision and Accuracy

Cloud optical parameters, in particular optical depth, are difficult to validate. Unlike other cloud parameters, cloud optical thickness is a radiative property. Thus, it is not possible to validate optical depth directly from in-situ measurements without making assumptions about the scattering of cloud particles.

Validating DCOMP products has been performed in several steps:

- Direct comparison with MODIS products. These retrievals use the same retrieval principle and therefore can be considered only as a sanity check.
- For liquid water clouds, the use of passive microwave retrievals from AMSR-E and SSM/I may help to validate the liquid water path.
- A-TRAIN measurements can help to identify aerosol layers that potentially falsify the results.

However, a first sanity check is the comparison with retrievals existing in the scientific community.

To estimate the precision and accuracy of DCOMP products, MODIS data from AQUA and TERRA satellite are used. To validate liquid water path, observations of passive microwave sensor AMSR-E are used. Inter-comparison with SEVIRI products of other research groups is an additional quality check.

4.2.2.1 Inter-comparison with Products of Other Research Groups

Validation strategies for optical parameters are rare. Therefore inter-comparison to other group's products are important consistency checks for newly introduced algorithms. The DCOMP algorithm was compared with its SEVIRI counterpart at the EUMETSAT workshop in Ascona, Switzerland in February 2009. Participants at this workshop were from 16 different institutions from Europe and North America. The comparison was a strict pixel-base 1:1 comparison for all cloud products. In this document, we only show a small subset of the workshop results.

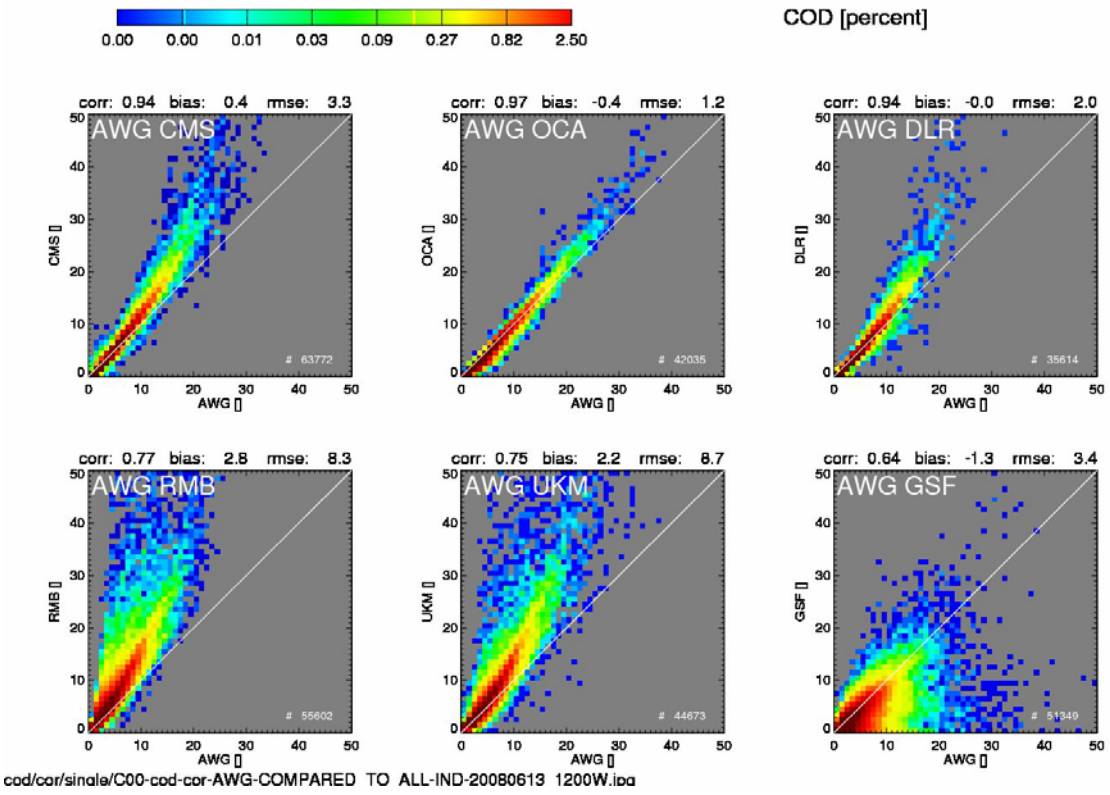

Figure 15. Comparison of DCOMP-COD for liquid water clouds algorithm (AWG) to six other groups.

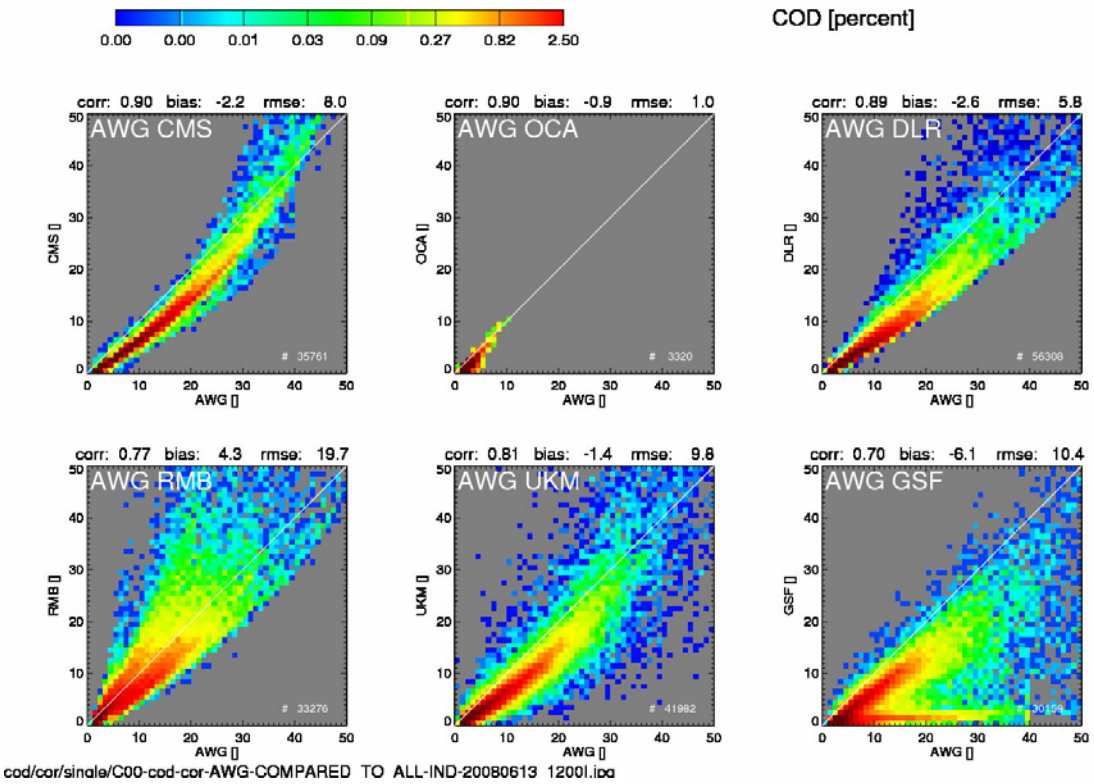

Figure 16. Comparison of DCOMP-COD Ice phase with six other groups.

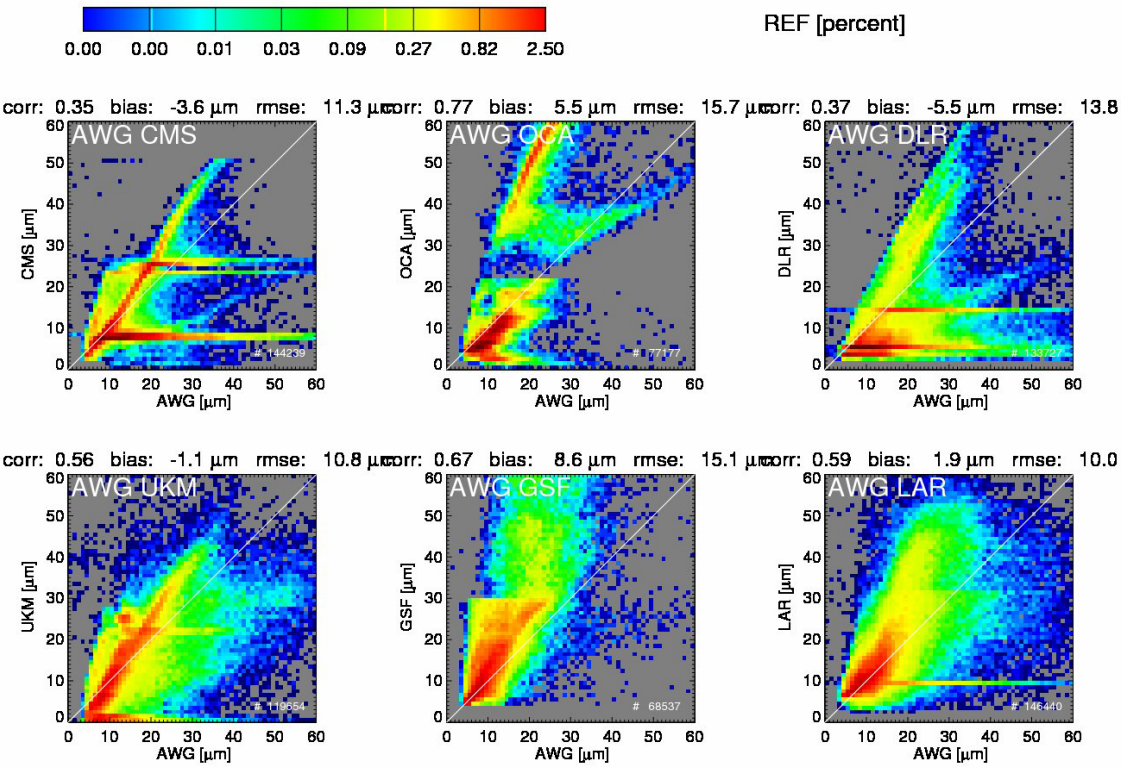

Figure 17. Comparison of DCOMP-REF all phases with six other groups.

Figure 15, Figure 16 and Figure 17 show the results of the comparison. The acronym "AWG" ("Algorithm Working Group") denotes the DCOMP algorithm. In all sub-images the DCOMP algorithm represents the x-axis of the 2D histograms. The other products are from EUMETSAT groups (CMS, OCA), the German Aerospace Center (DLR), the U.K. Met Office (UKM), Goddard Space Flight Center (GSFC) and from NASA Langley Research Center (LARC). These are not official products and might be also in a test phase.

Figure 15 summarizes the results for COD water retrieval. DCOMP shows excellent agreement with most other algorithms.

Figure 17 shows the all-phase results for Cloud Particle Size. In contrary to some other groups, DCOMP does not show peaks in the histograms. This potential artifact in non-AWG retrievals may be caused by underestimating of a-priori error.

4.2.2.2 Integrative Comparison with MODIS, AMSR-E along a CloudSat Track

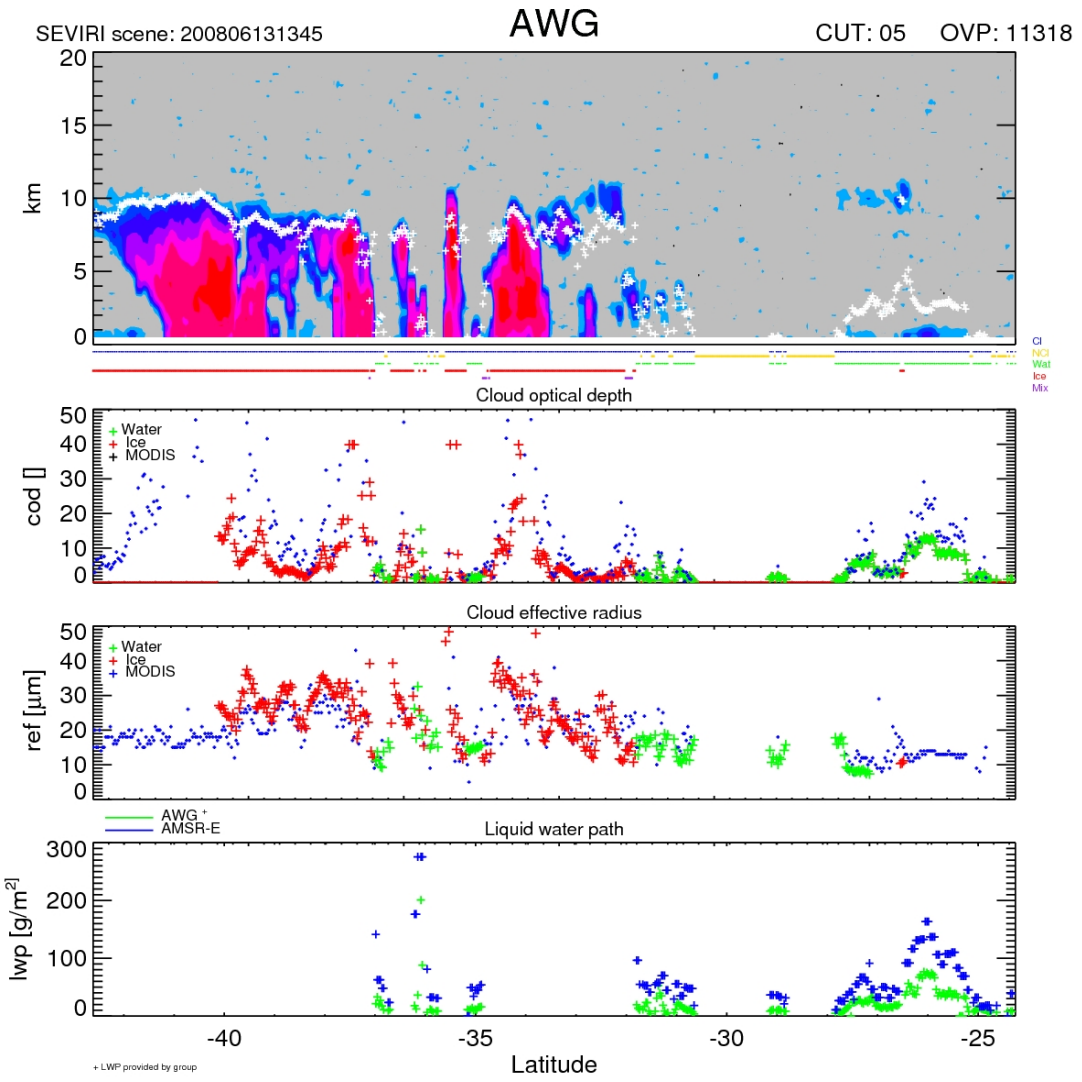

Figure 18. Integrative comparison of DCOMP products. Upper panel shows CloudSat radar reflectivities with ACHA cloud height (white crosses). Second panel shows comparison of DCOMP cloud optical depth of ice (red) and liquid water (green) with MODIS. Third panel shows same, but for effective radius. Bottom panel illustrates comparison of DCOMP liquid water path with AMSR-E.

The vertical profiles of radar reflectivity by CloudSat give a good opportunity to see in which situations the algorithm performs well and in which situations the algorithm has its weaknesses. In the upper panel of Figure 18 the CloudSat reflectance is shown with the result of the ACHA Cloud Height product. The Cloud height performs well for thicker clouds but performs poorly with multi-layer clouds at around 26S latitude. This may also impacts DCOMP because it uses the ACHA cloud height for atmospheric correction.

The other three panels are DCOMP product comparison with MODIS (image 2 and 3) and AMSR-E (4). Again, MODIS comparison does not represent a real validation, since it is measured with a similar observation and retrieval strategy. However, DCOMP shows here a good agreement to MODIS products.

An interesting comparison is the LWP check to AMSR-E data. Note, that only the liquid partition appears in this image, since AMSR-E, as all passive microwave sensors, only measures liquid water. Although the DCOMP product has systematically lower values, the variability in the time series seems to be reliable.

4.2.2.3 Long-period MODIS Analysis

The MODIS microphysical products (MYD06 and MOD06) have proven to be a useful and accurate source of information to the cloud remote sensing community. MODIS is a passive visible and infrared radiometer with a nominal spatial resolution of 1 km at nadir. In this comparison study we use the MODIS algorithm of cloud microphysical properties including cloud optical thickness, liquid and ice water path and cloud droplet effective radius. (Platnick 2003, King 2003)

MODIS level 2 cloud products are derived from a set of channels very similar to those used by DCOMP. Therefore, and in view of potential systematic error sources, comparisons between MODIS retrievals of cloud effective radius, cloud phase and cloud optical depth with corresponding DCOMP products should be performed with caution. Differences to MODIS products are not necessarily a sign of low quality of DCOMP products. It might be a result of the different approaches of the retrievals or the use of different ancillary data, such as the surface albedo, which could cause the differences

To compare the DCOMP results to those from MODIS, we analyzed MODIS data from AQUA and TERRA satellites that was nearly coincident with SEVIRI observations for a full ten days of data (days 230 to 239 in 2006). A 10-day time period provides a high number of matched observations in all possible weather situations. We do not expect a longer time period to show substantially different comparison results. We then compared these results to SEVIRI data that are closest in time. The time threshold is 2 minutes. The spatial threshold is 4 kilometers. We used only pixels in which both datasets have the same phase detected. In this analysis, only pixels where the 0.65 μm values agreed within 12% were used. The rationale for this criterion is that agreement of cloud products is only expected for pixels, which have rough agreement in the observations.

4.2.2.3.1 Comparison of Cloud Optical Depth

Figure 19 shows comparisons of the Cloud Optical Depth for water and ice with those SEVIRI and MODIS points that met all criteria described above. No additional filtering on the results was applied. The results indicate that the MODIS products were on average

1.59 units higher for water and 1.81 units higher for ice clouds. The corresponding precision values are 4.43 and 5.02 .

The agreement is particularly good for thin clouds. The biggest differences appear for water clouds with a cloud optical depth greater than 25. Note that the color bar is logarithmic stretched. The bulk number of matched points is within the depicted specs range.

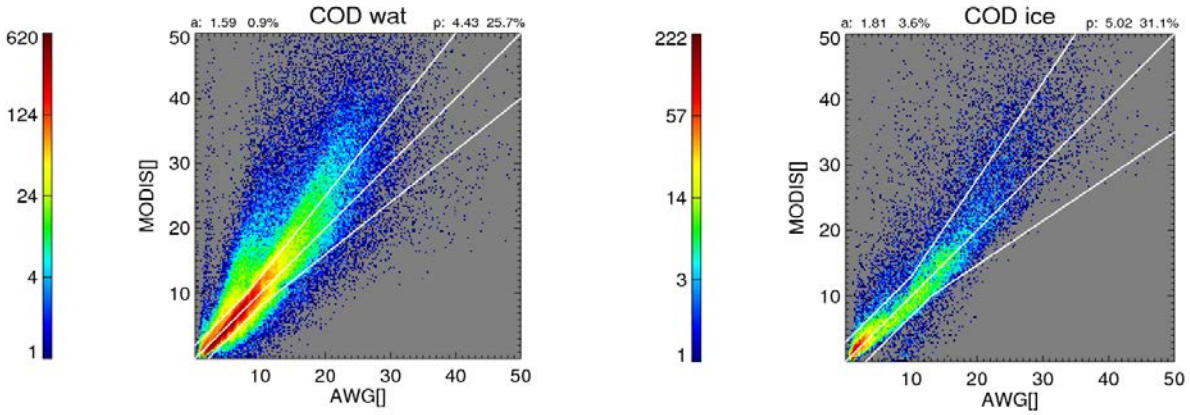

Figure 19. Comparison of Cloud Optical thickness for Days 230-239 in 2006 derived from MODIS (MYD06 and MOD06) products and from DCOMP algorithm. Left image shows results for water phase, right image for ice phase. Accuracy and precision of the comparison are shown in the figures. Specs ranges are added as white lines in the figures.

4.2.2.3.2 Comparison of Cloud Particle Size

Figure 20 shows the same comparison for Cloud Particle Size, referred to here as effective radius (REF). MODIS has mostly bigger values than DCOMP, but the comparison results are within the specs.

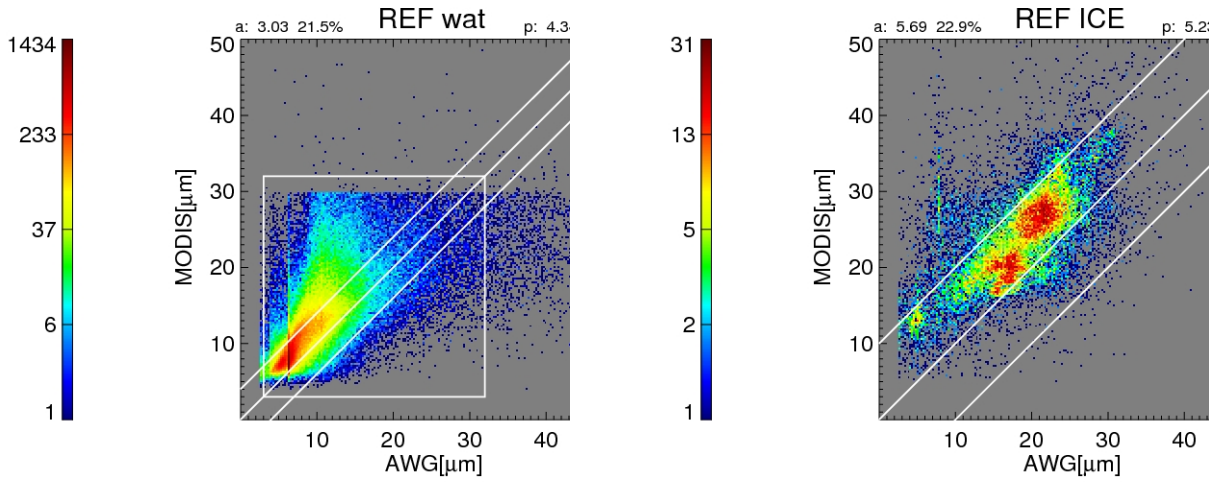

Figure 20. Comparison of Cloud Particle Size for Days 230-239 in 2006 derived from MODIS (MYD06 and MOD06) products and from DCOMP algorithm. Left image shows results for water phase, right image for ice phase. Accuracy and precision of the comparison are shown in the figures. Specs ranges are added as white lines in the figures.

4.2.2.3.3 Comparison of Cloud Liquid and Ice Liquid Path

For both retrievals, the water path is calculated directly from COD and CPS results under certain assumptions of the vertical profile of the cloud particle within the cloud. This approach can lead to bigger differences in a comparison study. Figure 21 shows the results for the 10-day period.

For LWP (left side) almost all pixels are in the specs range. However, there is a clear bias for parts of the LWP range. MODIS results show higher values of about 24 percent. The IWP image shows contrary comparison results. DCOMP has much higher values, up to 40 percent higher.

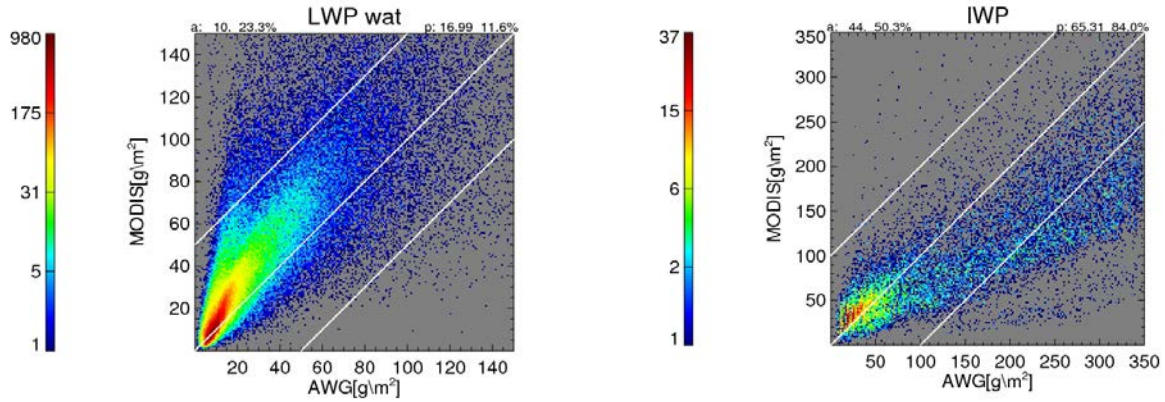

Figure 21. Comparison of Water Path for Days 230-239 in 2006 derived from MODIS (MYD06 and MOD06) products and from DCOMP algorithm. Left image shows results for water phase (LWP), right image for ice phase (IWP). Accuracy and precision of the comparison are shown in the figures. Specs ranges are added as white lines in the figures.

4.2.2.4 Comparison of DCOMP/LWP with AMSR-E

For liquid water path over ocean the passive satellite-based sensor AMSR-E offers a further validation data source. Limitations are different spatial resolution and the exclusive capability over sea and liquid phase. AMSR-E is a passive microwave radiometer onboard NASA's Aqua polar platform. It measures polarized radiances at six frequencies between 6 and 89 GHz.

We follow for this comparison studies from publications by Bennartz 2007, Greenwald 2009 and Juarez 2009. One AMSR-E pixel size is approx. 10x15 km. We use AMSR-E grid as "master" grid to which the "slave" grids of SEVIRI grid is matches. We apply the following matching criteria:

- 90 percent of the field of view of an AMSR-E pixel must be covered by liquid water clouds.
- Since AMSR-E observations are insensitive to thin clouds we exclude observations for COD lower than 5.
- To ensure that we really include only liquid clouds we apply a filter for clouds warmer than 268K.
- We flag out all AMSR-E pixels with a rain flag in quality flag output.

Spatial and temporal matching criteria are 5 kilometers spatial and 5 minutes time difference between the SEVIRI and AMSR-E measurement. For this comparison all SEVIRI pixels over the sea in a grid box with edges at 45E, 65S, 45W and 65N for 5 days in October 2006 and five days in April 2007 were considered.

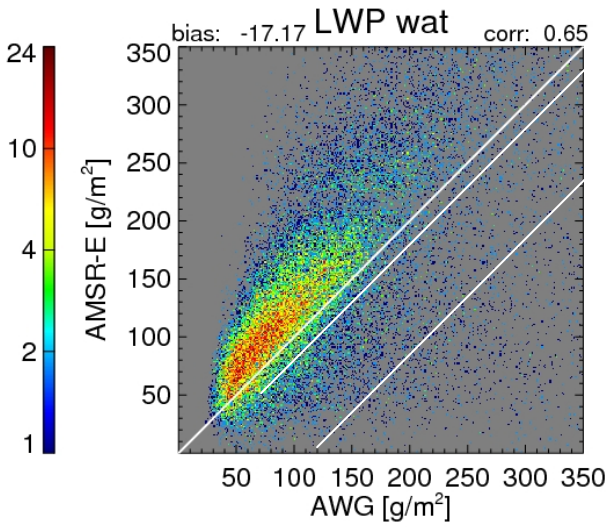

Figure 22. Comparison of AWG-DCOMP Liquid water product to AMSR-E for a two-day period (24-25August 2006) as a 2D histogram.

Figure 22 shows result for a 10-day period in October 2006 and April 2007. DCOMP (depicted as AWG in Figure 22) met the specification of 50 g/m2 for more than 90 percent of observations.

4.2.3 Error Budget

Using the validation described above, the following table provides our estimate of an error budget. DCOMP fulfilled the specifications of accuracy values for all validation data sets. The precision requirements were not met for three of the experiments. This result may be explained as follows:

The fact that the accuracy meets the specs, but not the precision, may be a result of frequent bad spatial and temporal matches between observations of two different satellites. Even in homogenous cloud regions, the difference can be significant especially for optical depth.

Calibration between MODIS and SEVIRI channels might be different.

The atmospheric correction is a function of cloud top pressure. Different CTPs might cause an additional error. A filtering regarding cloud top pressure was not applied.

Even though the LWP from the AMSR-E observations are the best available and physically reasoned data, the validation remains difficult due to different spatial resolution (5 km vs. 10/15 km).

Table 14 Error budget of DCOMP.

Product	Validation Source	Accuracy	Specs	Precision	Specs
COD Water	MODIS	1.59/0.9%	2. or 20%	4.43/25.7%	2. or 20%
COD Ice	MODIS	1.81/3.6%	3. or 30%	5.02/31.1%	3. or 30%
CPS Water	MODIS	3.03µm	4µm	4.3µm	4µm
CPS Ice	MODIS	5.69µm	10µm	5.23µm	10µm
LWP	MODIS	10g/m2	50 g/m2	17 g/m2	50 g/m2
LWP	AMSR-E	17 g/m2	50 g/m2	47 g/m2	50 g/m2
IWP	MODIS	44 g/m2	100 g/m2	65 g/m2	100 g/m2

4.2.4 DCOMP and the PATMOS-x AVHRR climate data set

DCOMP is a part of the climate data set PATMOS-x, which spans more than 30 years of AVHRR cloud observations on NOAA satellites. The generation of PATMOS-x level2b data is extensively described in Heidinger et al. 2013.

Cloud products are stored in a “level-2b” data format, which samples the cloud products in a regular 0.1 x 0.1 degree longitude/latitude grid. The sampling does not include any averaging, so that the algorithm space is conserved. Result is a handy and flexible climate data set, which makes it easy to investigate any climate questions concerning clouds and atmospheric parameters.

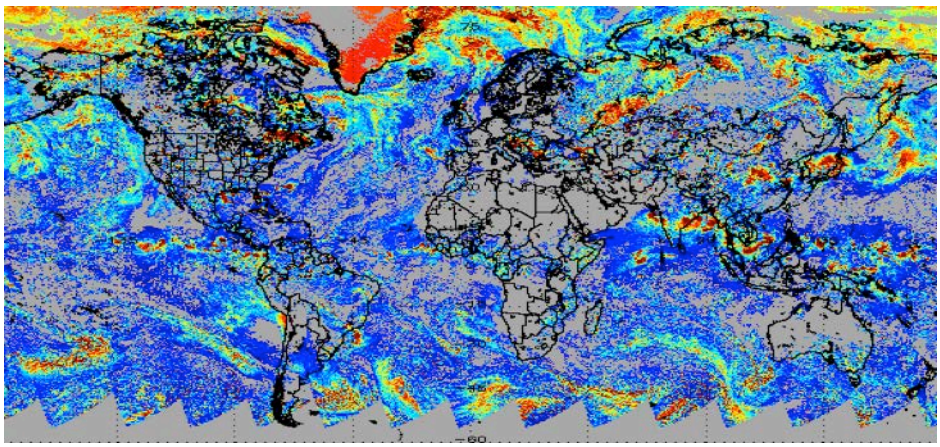

Figure 23. DCOMP Cloud Optical Thickness for one day of PATMOS-x level2b data from NOAA-18.

While the PATMOS-x data set was originally designed for NOAA satellite series, similar data sets are also generated for other appropriate sensors, such as MODIS, GOES and VIIRS. We use inter-comparison between multiple sensors as an additional evaluation of the performance and quality of DCOMP.

Figure 24. Comparison of level2b data from the AVHRR PATMOS-x data set (left) and a similar level-2b data set derived by GOES-EAST satellite

Figure 24 shows as an example the distribution of COD as a function of the derived cloud top pressure for one day of level2b data over the continental USA.

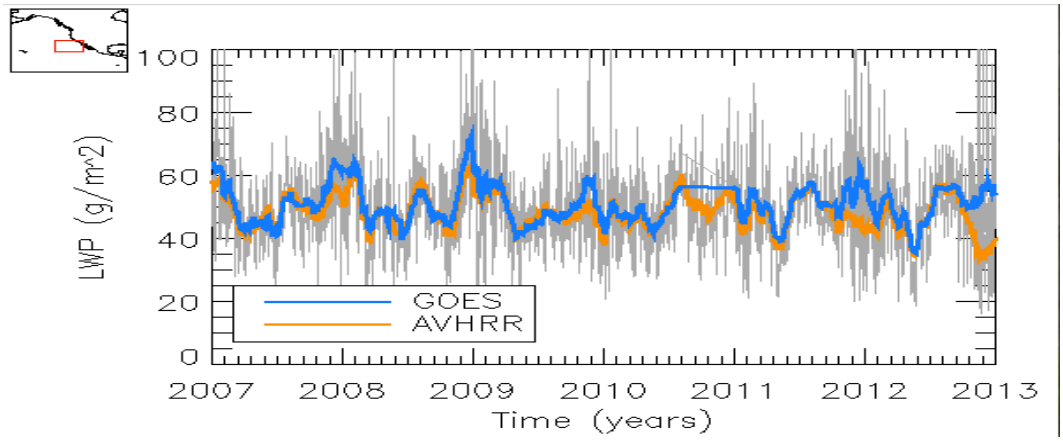

Figure 25. Time series of Liquid water path from DCOMP results in PATMOS-x data set in comparison to GOES-West results.

Figure 25 shows a time series of liquid water path derived by DCOMP over a part of Pacific Ocean off the Californian coast.

5. Practical Considerations

5.1 Numerical Computation Considerations

The algorithm is currently able to be implemented into CLAVRX framework and uses its numerical routines for processing. For SEVIRI proxy data (several data fields of 3712 x 3712 float elements) we run the algorithm on a 200 scan-line basis to avoid memory issues. The inversion process requires a large number (up to 50 times per pixel) of search events in look-up-tables. We explicitly paid attention on memory budget to speed up the code. The algorithm runs for a full SEVIRI scene in under five minutes.

5.2 Programming and Procedural Considerations

All code is written in the FORTRAN 90 programming language. It consists of one file with a FORTRAN *module* with several subroutines. An *include* file declares variable names of the software environment. It was tested to work in the framework environment.

The core algorithm is a pixel-by-pixel algorithm. The program interacts with the environment through data access subroutines. This program architecture makes it easy to run it in other ambient systems as well.

All input parameters that come from an external source are tested whether they fall in an expected and allowable range. All routine input parameters are also checked even if they come from another internal routine. Assertion code is included in each subroutine.

Global values were avoided as much as possible. Access to all variables from all subroutines is done by data access routine. We use pointer variables for output and several other parameters. Within the program we took care that all pointers' memory is freed.

5.3 Quality Assessment and Diagnostics

The following flags will be produced:

- Missing / No data
- Cloud-free
- Cloudy, but no convergence
- High value of cost function

5.4 Exception Handling

The algorithm checks the validity of each channel. The DCOMP algorithm also expects the main processing system to flag any pixels with missing geo-location or viewing geometry information.

The algorithm does check for conditions where the algorithm cannot be performed. These conditions include saturated channels or missing RTM values. In these cases, the appropriate flag is set to indicate that no value was produced for that pixel.

The following exception handlings are applied:

- If the MODIS surface albedo is missing, we use a default value (for land surfaces) of 0.15 instead.
- If NWP data are missing, we will use a default water vapor profile instead. This option is not currently implemented.

5.5 Algorithm Validation

It is recommended that comparisons to MODIS data remain the main validation tool for DCOMP.

5.6 Processing Environment and Resources

Processing and data generation resources used are located at The University of Wisconsin – Madison Space Science and Engineering Center (SSEC). Those resources include a Linux-based computing cluster using ~50 concurrent processors with a multi-node storage array containing sufficient space to store the PATMOS-x TCDR and FCDR as well as the precursor AVHRR Level1b and ancillary data products. Total space required is ~30TB. With the current hardware configuration we estimate we can process the entire AVHRR record and generate the PATMOS-x product in three weeks.

6. Assumptions and Limitations

The following sections describe the current limitations and assumptions in the current version of the DCOMP.

6.1 Algorithm Performance

The following assumptions have been made in developing and estimating the performance of the algorithm. The following list contains the current assumptions and proposed mitigation strategies.

1. NWP or reanalysis data of comparable or superior quality to the current 6 hourly CFSR data are available. (Use a default value for water vapor profile over clouds.)
2. Surface albedo values from MODIS are available for each pixel. (Use a default value.)
3. All of the static ancillary data are available at the pixel level. (Reduce the spatial resolution of the surface type, land mask and or coast mask.)
4. The processing system allows for processing of multiple pixels at once for application of the spatial uniformity tests. (No mitigation possible)
5. Visible channel is available. (No mitigation possible)
6. Near-IR channel is available. (No mitigation possible)

6.2 Sensor Performance

We assume the sensor will meet its current specifications. However, the DCOMP will be dependent on the following instrument characteristics.

- The spatial uniformity tests in the algorithm will be critically dependent on the amount of striping in the data.
- Unknown spectral shifts in some channels will cause biases in the clear-sky RTM calculations that may impact the performance of the algorithm.
- Errors in navigation from image to image will affect the performance of the temporal tests.

7. Future Enhancements

We have no product improvements planned at the moment.

8. Reference

Bennartz, R. (2007), Global assessment of marine boundary layer cloud droplet number concentration from satellite, *J Geophys Res-Atmos*, *112*(D2), -.

Greenwald (2009), A 2 year comparison of AMSR-E and MODIS cloud liquid water path observations, G*eophysical Research Letters,* 36, L20805, 6 PP., 2009

Hansen, J. E., and L. D. Travis (1974), Light-Scattering in Planetary Atmospheres, *Space Sci Rev*, *16*(4), 527-610.

Heidinger, A.K.; Foster, M.J.; Walther, A. The pathfinder atmospheres extended (PATMOS-x)

AVHRR climate data set. Bull. Am. Meteor. Soc. 2013, doi: 10.1175/BAMS-D-12-00246.1.

Heymsfield. (2003). Ice Water Path-Optical Relationships for Cirrus and Deep Stratiform Ice Cloud Layers, *J. Appl. Meteor.*, 42(10), 1369-1390.

Juarez, M., Kahn, B.H., Fetzer, E.J. (2009): Cloud-type dependencies of MODIS and AMSR-E liquid water path differences, *Atmospheric Chemistry and Physics*, 9, 3367-3399

King, M. D. (1987), Determination of the Scaled Optical-Thickness of Clouds from Reflected Solar-Radiation Measurements, *J Atmos Sci*, *44*(13), 1734-1751.

Mishchenko, M. I., et al. (1996), Sensitivity of cirrus cloud albedo, bidirectional reflectance and optical thickness retrieval accuracy to ice particle shape, *J Geophys Res-Atmos*, *101*(D12), 16973-16985.

Nakajima, T., and M. D. King (1990), Determination of the Optical-Thickness and Effective Particle Radius of Clouds from Reflected Solar-Radiation Measurements .1. Theory, *J Atmos Sci*, *47*(15), 1878-1893.

Nakajima, T., and M. D. King (1992), Asymptotic Theory for Optically Thick Layers - Application to the Discrete Ordinates Method, *Appl Optics*, *31*(36), 7669-7683.

Rodgers, C. D. (2000), *Inverse methods for atmospheric sounding : theory and practice*, xvi, 238 p. pp., World Scientific, Singapore ; [River Edge, N.J.].

Slingo, A. (1989), A Gcm Parameterization for the Shortwave Radiative Properties of Water Clouds, *J Atmos Sci*, *46*(10), 1419-1427.

Stephens, G. L. (1978), Radiation Profiles in Extended Water Clouds .1. Theory, *J Atmos Sci*, *35*(11), 2111-2122.

Van de Hulst (1974), Spherical Albedo of a Planet Covered with a Homogeneous Cloud Layer, *Astron Astrophys*, *35*(2), 209-214.

Wang, M. H., and M. D. King (1997), Correction of Rayleigh scattering effects in cloud optical thickness retrievals, *J Geophys Res-Atmos*, *102*(D22), 25915-25926.

Wiscombe, W. J. (1980), Improved Mie Scattering Algorithms, *Appl Optics*, *19*(9), 1505-1509.

GOES-R Algorithm Interface and Ancillary Data Description Document (AIADD)

GOES-R Series Ground Segment (GS) Project Functional and Performance Specification (F&PS) [G417-R-FPS-0089]

GOES-R ABI Cloud Mask Algorithm Theoretical Basis Document

GOES-R ABI Cloud Type/Phase Algorithm Theoretical Basis Document

GOES-R ABI Cloud Height Algorithm Theoretical Basis Document

GOES-R Level 1 Requirements Document (L1RD)

GOES-R Series Mission Requirements Document (MRD) [P417-R-MRD-0070]

GOES-R Acronym and Glossary (P417-R-LIST-0142)

.

Appendix A. Acronyms and Abbreviations

Acronym or Abbreviation	Meaning
C-ATBD	Climate Algorithm Theoretical Basis Document
CDR	Climate Data Record
NCDC	National Climatic Data Center
NOAA	National Oceanic and Atmospheric Administration
ABI	Advanced Baseline Imager
AIT	Algorithm Integration Team
AVHRR	Advanced Very High Resolution Radiometer
AWG	Algorithm Working Group
CALIPSO	Cloud-Aerosol Lidar and Infrared Pathfinder Satellite
CFSR	Climate Forecast System Reanalysis
CIMSS	Cooperative Institute for Meteorological Satellite Studies
DCOMP	Daytime Cloud Optical Microphysical Properties Algorithm
EUMETSAT	European Organization for the Exploitation of Meteorological Satellites
F&PS	Function and Performance Specification
GAC	Global Area Coverage
GFS	Global Forecast System
GOES	Geostationary Operational Environmental Satellite
IR	Infrared
MODIS	Moderate Resolution Imaging Spectroradiometer
MSG	Meteosat Second Generation
NASA	National Aeronautics and Space Administration
NCOMP	Nighttime Cloud Optical Microphysical Properties Algorithm
NOAA	National Oceanic and Atmospheric Administration
NWP	Numerical Weather Prediction
OE	Advanced Baseline Imager
RTM	Radiative transfer model
SEVIRI	Spinning Enhanced Visible and Infrared Imager
SSEC	Space Science and Engineering Center
STAR	Center for Satellite Applications and Research
UW	University of Wisconsin-Madison

VIS	Visible Range of Spectrum

Appendix B. Ancillary Data Sets

1. LAND_MASK_NASA_1KM

Description: Global 1km land/water used for MODIS collection 5

Filename: lw_geo_2001001_v03m.nc

Origin: Created by SSEC/CIMSS based on NASA MODIS collection 5

Size: 890 MB.

Static/Dynamic: Static

2. CFSR

Description: NCEP Climate Forecast System Reanalysis (CFSR) model data in hdf format – 0.5 x 0.5 degree (720x360), 26 levels

Filename: cfsr.YYMMDDHH_F006.hdf

Origin: NCEP cdas1.YYYYMMDD.pgrbh.tar

Size: 78MB

Static/Dynamic: Dynamic

3. SFC_ALBEDO

Description: MODIS White Sky Surface albedo

Filename: AlbMap.WS.c004.v2.0.YYYY.DDD.0.659_x4.nc

AlbMap.WS.c004.v2.0.YYYY.DDD.1.64_x4.nc

Origin:

Size: **2**8 MB x 2

Static/Dynamic: Static

4. SFC_TYPE_AVHRR_1KM

Description: Surface type mask based on AVHRR at 1km resolution

Filename: gl-latlong-1km-landcover.nc

Origin: University of Maryland

Size: 890 MB

Static/Dynamic: Static